



A genetic map of the mouse dorsal vagal complex and its role in obesity

Mette Q. Ludwig¹, Wenwen Cheng¹, Desiree Gordian², Julie Lee³, Sarah J. Paulsen⁴, Stine N. Hansen⁴, Kristoffer L. Egerod¹, Pernille Barkholt¹⁵, Christopher J. Rhodes¹⁶, Anna Secher¹⁴, Lotte Bjerre Knudsen¹⁴, Charles Pyke⁴, Martin G. Myers Jr² and Tune H. Pers¹[✉]

The brainstem dorsal vagal complex (DVC) is known to regulate energy balance and is the target of appetite-suppressing hormones, such as glucagon-like peptide 1 (GLP-1). Here we provide a comprehensive genetic map of the DVC and identify neuronal populations that control feeding. Combining bulk and single-nucleus gene expression and chromatin profiling of DVC cells, we reveal 25 neuronal populations with unique transcriptional and chromatin accessibility landscapes and peptide receptor expression profiles. GLP-1 receptor (GLP-1R) agonist administration induces gene expression alterations specific to two distinct sets of *Glp1r* neurons—one population in the area postrema and one in the nucleus of the solitary tract that also expresses calcitonin receptor (*Calcr*). Transcripts and regions of accessible chromatin near obesity-associated genetic variants are enriched in the area postrema and the nucleus of the solitary tract neurons that express *Glp1r* and/or *Calcr*, and activating several of these neuronal populations decreases feeding in rodents. Thus, DVC neuronal populations associated with obesity predisposition suppress feeding and may represent therapeutic targets for obesity.

Despite the increasing incidence and prevalence of obesity and obesity-related complications across the globe, effective treatments remain scarce^{1,2}. A variety of data suggest the importance of central nervous system (CNS) pathways for the control of body weight and in susceptibility to and treatment of obesity³. Not only do CNS pathways mediate the effects of a variety of monogenic obesity alleles⁴, but most weight-lowering pharmacotherapeutics act in the brain⁵. Furthermore, genetic variants associated with body mass index (BMI), a surrogate for obesity, identified in genome-wide association studies (GWAS) map predominantly to CNS-expressed genes^{6,7}.

Within the CNS, the brainstem DVC—composed of the area postrema (AP), the nucleus of the solitary tract (NTS) and the dorsal motor nucleus of the vagus nerve (DMV)—plays important roles in integrating peripheral satiety signals and regulating energy balance⁸. Indeed, the AP (a circumventricular organ that lacks a blood–brain barrier and thus directly senses blood-borne signals) and adjacent NTS express a variety of receptors that suppress feeding, including GLP-1 receptor (*Glp1r*)^{9,10}, GDNF family receptor alpha-like (*Gfral*)¹¹, calcitonin receptor (*Calcr*), amylin receptor (a calcitonin receptor and receptor activity-modifying protein (*Ramp*) heterodimer)¹² and gastric inhibitory polypeptide receptor (*Gipr*)¹³. The AP and NTS contribute to the anorexic effects of amylin and GLP-1R agonists (GLP-1RAs)^{14–16}, respectively, and both the AP and NTS are involved in salmon calcitonin (sCT)-induced food suppression^{14,17,18}. Furthermore, *Calcr* neurons in the NTS contribute to the physiological control of feeding and body weight¹⁷. Hence, neurons in the DVC represent likely targets for therapeutic intervention in obesity. It will be important to agnostically and comprehensively understand the identities and heterogeneity of DVC cell populations and to understand potential

DVC controllers of food intake and body weight to define potential therapeutic targets for obesity.

Large-scale assessment of cellular heterogeneity and the unbiased identification of cell populations require single-cell profiling techniques, such as single-nucleus RNA-sequencing (snRNA-seq) and single-nucleus assay for transposase-accessible chromatin by sequencing (snATAC-seq)¹⁹. These techniques not only permit comprehensive mapping of cell populations by their genetic signatures but can also reveal cell population-specific responses to pharmacological treatments²⁰. When integrated with GWAS data, these cellular atlases can also be leveraged to agnostically nominate candidate cell populations and regulatory networks mediating susceptibility to complex traits and disease (including obesity)^{7,21,22}.

Here, we identify specific DVC cell populations that control energy balance. We combined data from bulk RNA-seq with snRNA-seq and snATAC-seq from the mouse AP and surrounding DVC to construct transcriptional and chromatin accessibility atlases of DVC cell populations. In addition, we identify DVC cell population-specific responses to anorectic GLP-1RA administration and utilize BMI GWAS data to identify DVC cell populations that likely contribute to obesity predisposition. We demonstrate that two of these neuronal populations (one expressing the amylin receptor complex and another expressing *Calcr* and *Glp1r*) can control food intake, consistent with their potential utility as targets for therapeutic intervention in obesity.

Results

RNA-seq of areas activated by GLP-1 receptor agonist administration. The GLP-1RA liraglutide represents one of the most effective pharmacological treatments currently available for obesity⁵, and the more long-acting and potent GLP-1RA semaglutide has been

¹Novo Nordisk Foundation Center for Basic Metabolic Research, University of Copenhagen, Copenhagen, Denmark. ²Department of Internal Medicine, University of Michigan, Ann Arbor, MI, USA. ³Novo Nordisk Foundation Center for Stem Cell Biology, University of Copenhagen, Copenhagen, Denmark.

⁴Global Drug Discovery, Novo Nordisk A/S, Måløv, Denmark. ⁵Gubra, Hørsholm, Denmark. ⁶Research and Early Development, Cardiovascular, Renal and Metabolic Diseases, BioPharmaceuticals R&D, AstraZeneca, Gaithersburg, MD, USA. [✉]e-mail: tune.pers@sund.ku.dk

submitted for regulatory approval following completed phase III clinical trials²³. Glutamatergic *Glp1r* neurons likely mediate GLP-1RA effects on feeding and body weight²⁴, and GLP-1RAs engage cells in the hypothalamus (including in the arcuate nucleus of the hypothalamus (ARH), dorsomedial nucleus of the hypothalamus (DMH) and paraventricular nucleus of the hypothalamus (PVH)), the lateral septum (LS), the AP (tyrosine hydroxylase (TH) neurons) and the NTS²⁵. However, we lack a more complete understanding about cell population-specific responses to GLP-1RAs in general and potential differences in the responses to individual GLP-1RAs.

To understand the transcriptional response to GLP-1RA administration, we randomized diet-induced obese (DIO) male mice into four groups: (1) semaglutide-administered, (2) liraglutide-administered, (3) ad libitum-fed vehicle-administered and (4) weight-matched controls (to discriminate between weight loss effects induced by GLP-1RA administration and food restriction; Fig. 1a). Semaglutide was administered at a lower dose than liraglutide to obtain similar effects on weight loss. Mice were dosed once daily for 7 d and, as expected, the semaglutide- and liraglutide-administered groups lost weight during treatment (10.34 ± 0.59 g and 8.7 ± 0.46 g (mean \pm s.e.m.), respectively) relative to baseline, corresponding to a 18% and 15.5% reduction in body weight, respectively (Fig. 1b). The amount of food given to the weight-matched group was lower than that in the GLP-1RA-administered groups, suggesting a reduction in energy expenditure in the weight-matched group compared to the GLP-1RA-administered groups, consistent with previous observations²⁵ (Fig. 1c).

Following treatment, we used laser capture microscopy to dissect relevant brain areas and identify global patterns of differential gene expression using bulk RNA-seq. Following data normalization and quality-control filtering, we performed principal component analysis (PCA), revealing that samples clustered by brain area and developmental compartment (Fig. 1d). Of the brain areas examined, the AP exhibited the largest number of differentially expressed genes between the GLP-1RA-administered mice and weight-matched controls (Benjamini–Hochberg (BH)-adjusted $P < 0.05$; Fig. 1e and Supplementary Data 1). Apart from only one and two differentially expressed genes in the LS and DMH, respectively, we found no significant differences between the semaglutide- and liraglutide-induced transcriptional changes, suggesting that the two GLP-1RAs have similar transcriptional consequences in the six brain areas investigated (Fig. 1f and Supplementary Data 1); we thus focused subsequent analyses on semaglutide-administered animals. Among the most upregulated genes in the AP from semaglutide-administered animals, many encoded neurotrophins and neuropeptides, including growth hormone-releasing hormone (*Ghrh*), VGF nerve growth factor inducible (*Vgf*), CART prepropeptide (*Cartpt*) and prodynorphin (*Pdyn*), suggesting that GLP-1RA administration alters neuronal function and neurotransmission in the AP (Fig. 1g).

Transcriptional single-cell atlas of the dorsal vagal complex. Directing our attention to the AP and adjacent areas, we investigated whether distinct cell populations could represent potential targets of GLP-1RAs and other therapeutics of obesity. To that end, we subjected DVC tissue from AP-centred dissections from (1) semaglutide-administered, (2) ad libitum-fed vehicle-administered and (3) weight-matched control DIO mice (replicating the previous *in vivo* set-up) to snRNA-seq (Fig. 2a and Extended Data Fig. 1). The quality-controlled dataset contained a total of 72,128 cells consisting of 49,392 neurons and 22,736 glial cells distributed across eight distinct cell types (Fig. 2b,c). Marker genes for all cell populations were identified using the CELLEX tool⁷, computing a combined expression specificity measure (ES_{μ} ; range (0,1); low to high cell population specificity) across four individual metrics (Supplementary Data 2). One glial cell population could not easily be assigned a label based on known marker genes and turned out to be similar

to tanycytes when compared with a published ARH–median eminence (ME) single-cell atlas²² (henceforth ‘tanyocyte-like’ cells²⁶). Top marker genes of these tanyocyte-like cells included Wilms tumour 1 homologue (*Wt1*), Wnt inhibitory factor 1 (*Wif1*), solute carrier family 22 member 3 (*Slc22a3*) and cell adhesion molecule-related/downregulated by oncogenes (*Cdon*; Supplementary Data 2), all of which were highly specific to the AP but not restricted to the ventricles when cross-referenced with *in situ* hybridization (ISH) data from the Allen Mouse Brain Atlas²⁷ (Extended Data Fig. 2). We conclude that tanyocyte-like cells represent a unique glial cell population in the AP, although the exact identity of these cells warrants further exploration.

By reclustering all neurons using a measure of cluster cohesiveness to determine the optimal number of clusters, we identified 25 neuronal populations (Fig. 2d and Supplementary Data 2). Because our dissections included cells from the AP, NTS and DMV, we sought to determine the most plausible origin of the different cell populations. Using the laser capture microscopy-dissected bulk RNA-seq data, we identified neuronal populations that were enriched for genes with differential expression between the AP and NTS. These data, along with manual curation using the Allen Mouse Brain Atlas, allowed us to assign five populations of neurons to the AP, 15 to the NTS and five to the DMV (Fig. 2e, Extended Data Fig. 3 and Supplementary Data 3).

The DVC contains GABAergic, glutamatergic and catecholaminergic (dopaminergic and noradrenergic) neurons^{10,24,28}. Examining the expression of the vesicular GABA transporter (*Slc32a1*) and the vesicular glutamate transporter 2 (*Slc17a6*), we detected an abundance of glutamatergic neurons (*Glu1–15*) over GABAergic neurons (GABA1–7; Fig. 2f). Assessing the expression of tyrosine hydroxylase (*Th*), dopamine decarboxylase (*Ddc*) and dopamine beta hydroxylase (*Dbh*) as markers for dopaminergic (*Th*^{+/+}/*Ddc*^{+/+}/*Dbh*^{-/-}) and noradrenergic (*Th*^{+/+}/*Ddc*^{+/+}/*Dbh*^{+/+}) neurons, we further identified several populations of catecholaminergic neurons, all of which were also glutamatergic; one population expressed dopaminergic markers (*Glu7*^{NTS}), and four expressed noradrenergic markers (*Glu2*^{NTS}, *Glu4*^{AP}, *Glu5*^{NTS} and *Glu11*^{NTS}). Additionally, using the marker choline O-acetyltransferase (*Chat*), we identified three cholinergic neuronal populations (*Chat1–3*), of which two also expressed dopaminergic markers (*Chat1*^{DMV} and *Chat3*^{DMV}; Fig. 2f). Together, these results demonstrate a transcriptionally diverse organization of non-neuronal and neuronal cells in the AP, NTS and DMV.

Expression of appetite-suppressing genes across cell populations. To understand DVC cell populations that potentially are involved in energy balance control, we examined the expression of *Glp1r* along with other anorexic receptors and peptides across DVC cell populations. Despite the reportedly high expression of *Glp1r* in the AP^{9,10}, we were initially unable to identify *Glp1r* populations. By remapping the genome annotation to include reads falling within downstream alternative polyadenylation (poly(A)) signals and recomputing the transcript counts for *Glp1r*, we identified three neuronal populations with high expression specificities of *Glp1r*; GABA7^{AP} ($ES_{\mu} = 0.72$), *Glu4*^{AP} ($ES_{\mu} = 0.99$) and *Glu11*^{NTS} neurons ($ES_{\mu} = 0.64$; Fig. 3a,b and Supplementary Data 2).

We observed an overlap between neuronal populations expressing *Glp1r* and two other receptors known to be involved in DVC body weight control, namely *Gfral* and *Calcr* (Fig. 3b and Supplementary Data 2). *Glu4*^{AP} (*Glp1r*) and non-*Glp1r* *Glu5*^{NTS} and *Glu13*^{NTS} neurons expressed *Gfral* ($ES_{\mu} = 0.99$, $ES_{\mu} = 0.96$ and $ES_{\mu} = 0.73$, respectively). We confirmed with immunohistochemistry (IHC) and ISH in mice and non-human primate samples that a subset of cells in the AP but not in the NTS coexpressed *Glp1r* and *Gfral* (Fig. 3c and Extended Data Fig. 4a). *Calcr* was expressed by *Glu11*^{NTS} (*Glp1r*), *Glu2*^{NTS} and *Glu10*^{AP} neurons ($ES_{\mu} = 0.91$, $ES_{\mu} = 0.56$ and $ES_{\mu} = 0.99$, respectively), and by applying double (db)-ISH in mice and

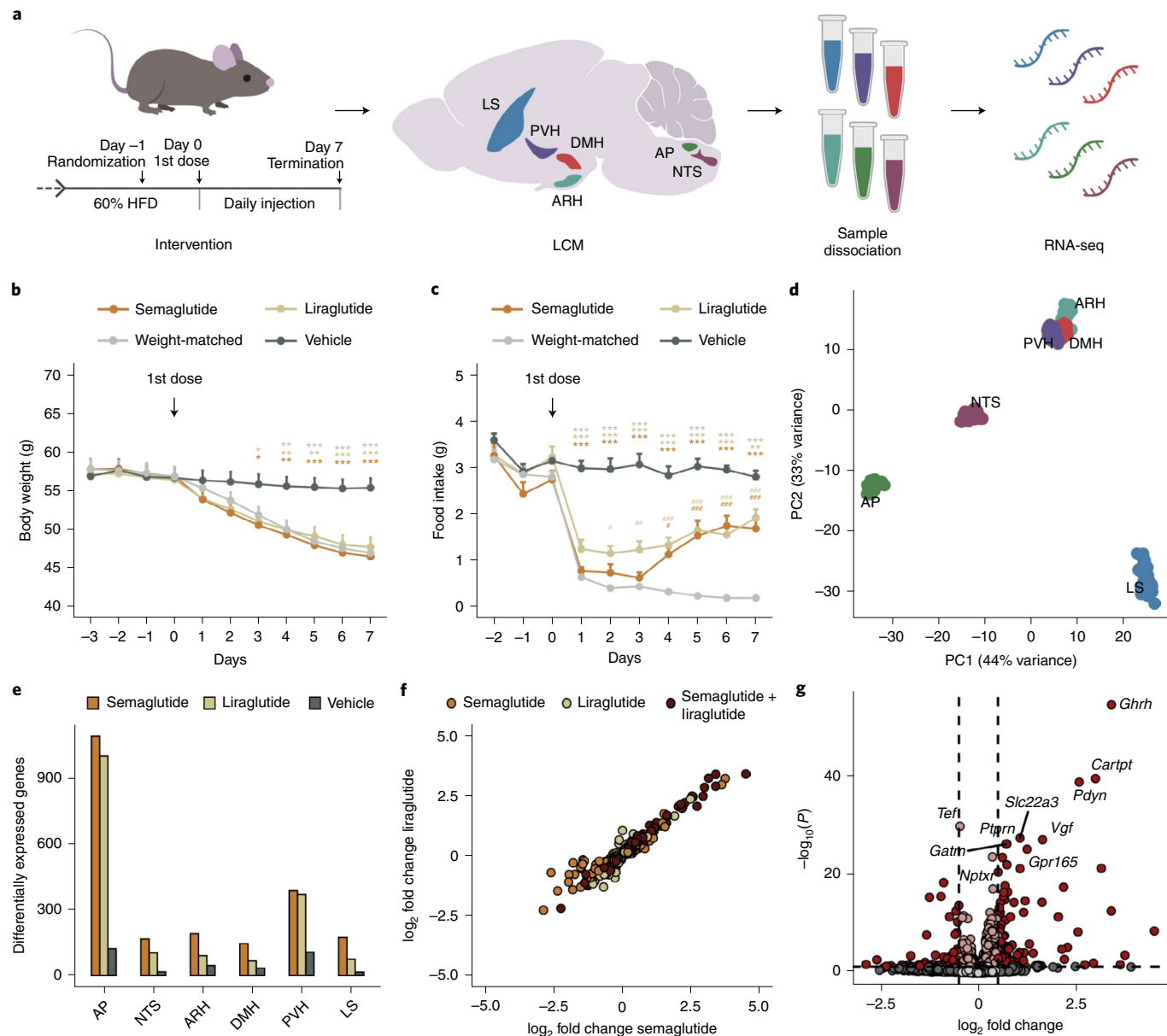


Fig. 1 | Overview of transcriptional changes in response to GLP-1 receptor agonist administration. **a**, Overview of bulk RNA-seq study design. DIO mice were randomized into four groups: semaglutide-administered (all subcutaneous (s.c.); day 0, 0.02 mg kg⁻¹; day 1, 0.04 mg kg⁻¹; days 2–6, 0.1 mg kg⁻¹; $n=15$), liraglutide-administered (all s.c.; day 0, 0.2 mg kg⁻¹; day 1, 0.4 mg kg⁻¹; days 2–6, 1.0 mg kg⁻¹; $n=15$), ad libitum-fed vehicle-administered ($n=15$) and weight-matched controls ($n=15$). Animals were dosed once daily for 7 d. Six brain areas were isolated with laser capture microscopy, dissociated and subjected to RNA-seq. **b,c**, Daily body weight (**b**) and food intake (**c**) following GLP-1RA administration ($n=15$ mice per group). Values are the mean \pm s.e.m. * $P<0.05$, ** $P<0.01$, *** $P<0.001$ versus vehicle and # $P<0.05$, ## $P<0.01$, ### $P<0.001$ for semaglutide and liraglutide versus weight-matched controls; linear mixed-effects model and Bonferroni-adjusted least-squares means two-tailed *t*-test. **d**, PCA plot of samples coloured by brain area. **e**, Number of differentially expressed genes compared to weight-matched animals. BH-adjusted DESeq2 $P<0.05$. **f**, \log_2 fold changes of differentially expressed genes for semaglutide- and liraglutide-administered animals versus weight-matched animals. Dark red indicates a \log_2 fold change >0.5 and BH-adjusted DESeq2 $P<0.05$. The top ten significant genes are labelled. HFD, high-fat diet; PC, principal component. Data for reconstruction of **d–g** are available in Supplementary Data 1 and at the NCBI Gene Expression Omnibus (GEO).

non-human primates, we validated that *Calcr* colocalized with the majority of *Glp1r* cells in the NTS; in contrast, few *Glp1r* cells coexpressed *Calcr* in the AP (Fig. 3d and Extended Data Fig. 4b). The top marker genes for Glu4^{AP} (*Glp1r/Gfral*) and Glu11^{NTS} (*Glp1r/Calcr*) neurons were calcium-sensing receptor (*Casr*) and gastrin-releasing peptide receptor (*Grpr*), respectively (Fig. 2f). The coexpression of *Casr* and *Glp1r* in the AP matched our db-ISH data in mice and non-human primates, as did the coexpression of *Grpr* with *Glp1r*

and *Calcr* in the NTS (Fig. 3e,f and Extended Data Fig. 4c,d). Two other anorexic genes were expressed in Glu4^{AP} (*Glp1r/Gfral*) and Glu11^{NTS} (*Glp1r/Calcr*) neurons, namely brain-derived neurotrophic factor (*Bdnf*; $ES_\mu=0.94$ and $ES_\mu=0.89$, respectively) and melanocortin 4 receptor (*Mc4r*; $ES_\mu=0.43$ and $ES_\mu=0.94$, respectively; Fig. 3b). By applying db-ISH, we validated the colocalization of *Casr* and *Bdnf* in the AP and the colocalization of *Grpr* with *Bdnf* and *Mc4r* in the NTS, although we were unable to detect any

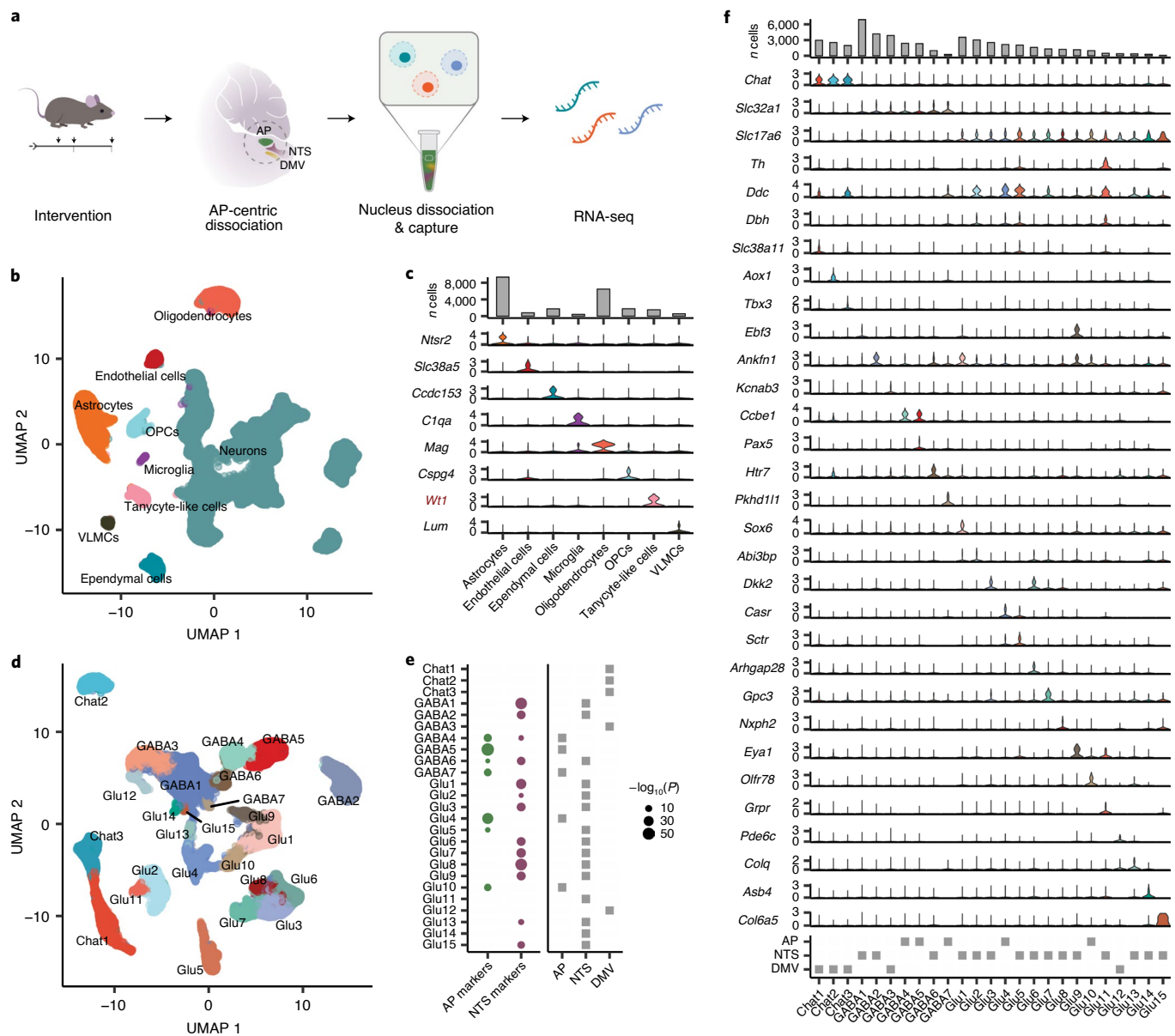


Fig. 2 | Transcriptional atlas of DVC cell populations. **a**, Overview of snRNA-seq study design. DIO mice were randomized into three groups: semaglutide-administered ($n=7$), ad libitum-fed vehicle-administered ($n=6$) and weight-matched controls ($n=7$). Animals were dosed once daily for 7 d as described for the bulk RNA-seq in vivo study. The AP, NTS and DMV were dissociated and subjected to snRNA-seq. **b**, Uniform manifold approximation and projection (UMAP) plot of 72,128 cells coloured by cell type. **c**, Non-neuronal marker genes. Top, number of cells per cluster. Bottom, violin plot showing the normalized transcript counts for marker genes. A black label indicates that the gene is also a marker of the cell type in the hypothalamus, and a red label indicates lack of specificity in the hypothalamus. **d**, UMAP plot of 49,392 neurons coloured by population. **e**, Enrichment of AP and NTS marker genes. Left, dots indicate the significance level of overlap between AP and NTS marker genes and cell population marker genes ($ES_\mu > 0$). Bonferroni-adjusted one-tailed Fisher's exact test. Right, the most likely DVC origin of the cell populations. **f**, Neuronal marker genes. From top to bottom: number of cells per cluster, violin plots of the normalized transcript count for marker genes and the most likely DVC origin of the neuronal populations. *Chat*, *Slc32a1*, *Slc17a6*, *Th*, *Ddc* and *Dbh* were used as markers for neurotransmitter subtypes. OPCs, oligodendrocyte precursor cells. Data for reconstruction of **b–f** are available in Supplementary Data 2 and 3 and at NCBI GEO.

Mc4r expression in the AP of control mice (Extended Data Fig. 4e–h). Finally, Glu4^{AP} (*Glp1r/Gfral*) and $\text{Glu11}^{\text{NTS}}$ (*Glp1r/Calcr*) neurons specifically expressed the three components to synthesize noradrenaline, namely *Th* ($ES_\mu = 0.49$ and $ES_\mu = 0.96$, respectively), *Ddc* ($ES_\mu = 0.97$ and $ES_\mu = 0.63$, respectively) and *Dbh* ($ES_\mu = 0.83$ and $ES_\mu = 0.90$, respectively), findings which we replicated for *Th* and *Ddc* with IHC experiments in *Glp1r-Cre* and *Calcr-Cre* mice (Extended Data Fig. 4i–l). Together, these results identify noradrenergic *Glp1r* neurons in the AP and NTS of mice and non-human

primates that express receptors capable of sensing distinct, but overlapping, anorectic signals.

We also detected appetite-regulating receptors in cell populations that did not express *Glp1r* and *Gfral*. Glu10^{AP} (*Calcr*) neurons expressed *Ramp3* ($ES_\mu = 0.99$; Fig. 3b and Supplementary Data 2). The top marker of this population was olfactory receptor 78 (*Olf78*; Fig. 2f), and the coexpression of *Calcr* with *Ramp3* and *Olf78* exclusively in the AP aligned with our IHC and ISH data in mice and non-human primates (Fig. 3g,h and Extended Data Fig. 5a).

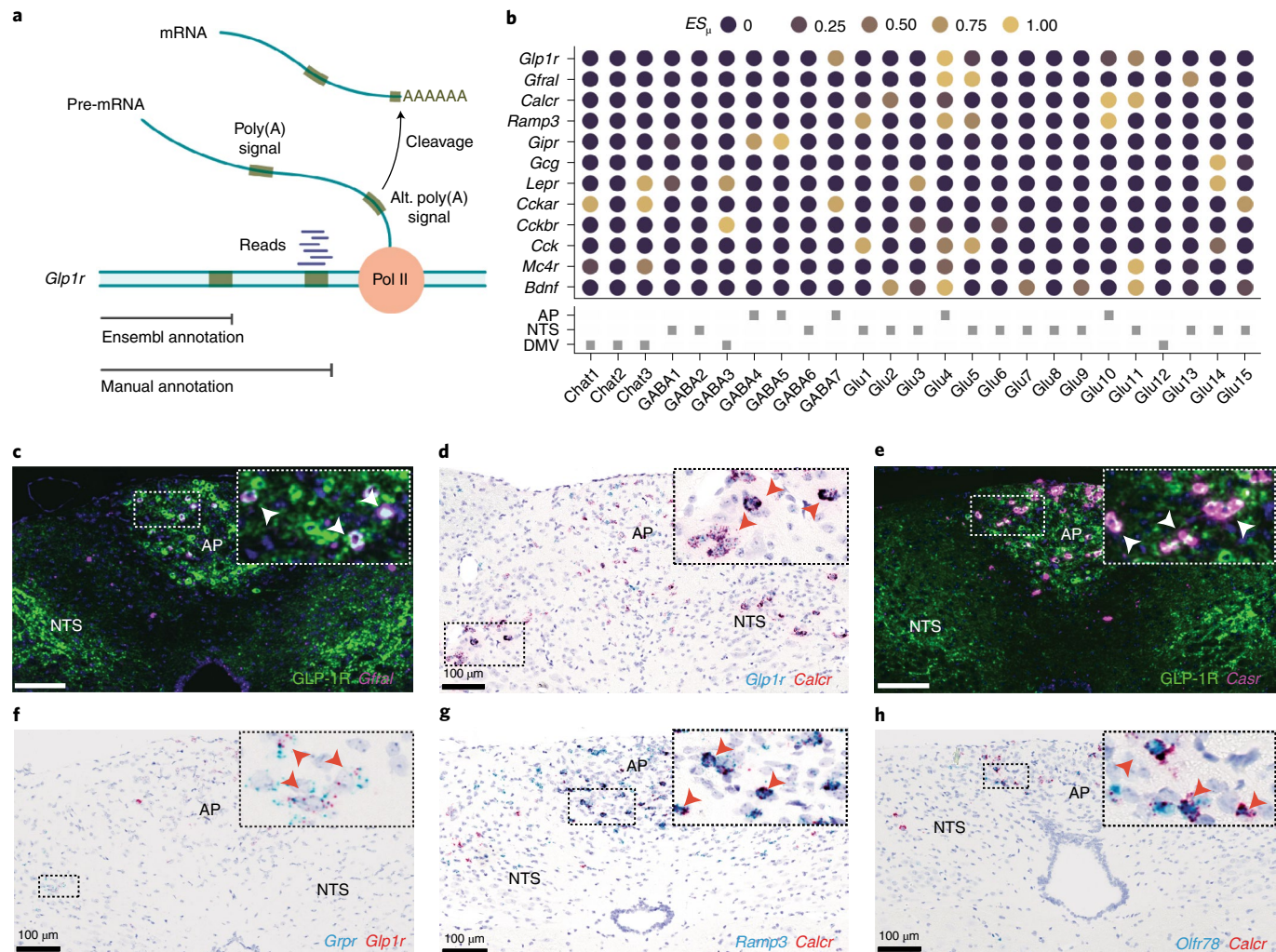


Fig. 3 | Neuronal expression of receptors and peptides involved in body weight control. **a**, Overview of *Glp1r* gene re-annotation. The transcript counts for *Glp1r* were computed following manual re-annotation to include alternative poly(A) signals. **b**, Cell population expression specificities (ES_p) of selected genes. Bottom, the most likely DVC origin of the neuronal populations. **c**, Representative image showing combined IHC of GLP-1R (green) and ISH of *Gfral* (magenta; $n=3$). **d**, Representative image showing double (db)-ISH of *Glp1r* (blue) and *Calcr* (red; $n=3$). **e**, Representative image showing combined IHC of GLP-1R (green) and ISH of *Casr* (magenta; $n=3$). **f**, Representative image showing db-ISH of *Grpr* (blue) and *Glp1r* (red; $n=4$). **g**, Representative image showing db-ISH of *Ramp3* (blue) and *Calcr* (red; $n=3$). **h**, Representative image showing db-ISH of *Olfr78* (blue) and *Calcr* (red; $n=4$). Arrows in **c–h** denote cells with colocalization. Scale bars for **c–h** represent 100 μ m. pol II, RNA polymerase II. Data for reconstruction of **b** are available in Supplementary Data 2.

This further corroborates that Glu10^{AP} (*Calcr/Ramp3*) neurons represent an amylin-sensing neuronal population. In addition, GABA4^{AP} and GABA5^{AP} neurons expressed *Gipr* ($ES_p=0.79$ and $ES_p=0.98$, respectively; Fig. 3b). Collagen- and calcium-binding EGF domain-containing protein 1 (*Ccbe1*) was the top marker of GABA4^{AP} neurons and also specifically expressed in GABA5^{AP} neurons ($ES_p=0.97$), while paired box 5 (*Pax5*) was the top marker of GABA5^{AP} neurons (Fig. 2f). By applying db-ISH, we validated that a subset of *Ccbe1* and the majority of *Pax5* cells colocalized with *Gipr* in the AP (Extended Data Fig. 5b,c). We also verified that *Gipr* and *Glp1r* were expressed in nonoverlapping AP cells (Extended Data Fig. 5d). These results demonstrate that the partially overlapping expression of receptors for anorexic peptides are distributed across several distinct neuronal cell populations in the DVC of mice and non-human primates.

Furthermore, the NTS is known to comprise a small population of preproglucagon (*Gcg*)-expressing neurons encoding a precursor peptide for GLP-1 (ref. ²⁹). Indeed, we detected high expression of

Gcg in Glu14^{NTS} neurons ($ES_p=0.95$; Fig. 3b and Supplementary Data 2). In line with previous observations, this population also expressed the leptin receptor (*Lepr*; $ES_p=0.92$; Fig. 3b)³⁰. The top marker gene of Glu14^{NTS} neurons was ankyrin repeat and SOCS box-containing 4 (*Asb4*; known to be highly expressed and regulated in *Lepr*-expressing neurons³¹), consistent with our db-ISH data (Fig. 2f and Extended Data Fig. 5e). Finally, we were able to map additional DVC cell populations with previously defined roles in metabolism onto our atlas (Extended Data Fig. 6).

Transcriptional programmes induced by GLP-1 receptor agonists. To better understand the transcriptional response to GLP-1RA administration in AP and neighbouring DVC cells, we applied weighted gene coexpression network analysis (WGCNA; a computational approach to identify sets of co-regulated genes associated with treatment outcomes) on bulk RNA-seq data from the AP. In total, we identified 23 gene modules (M1–M23), four of which were associated with semaglutide administration (module M1

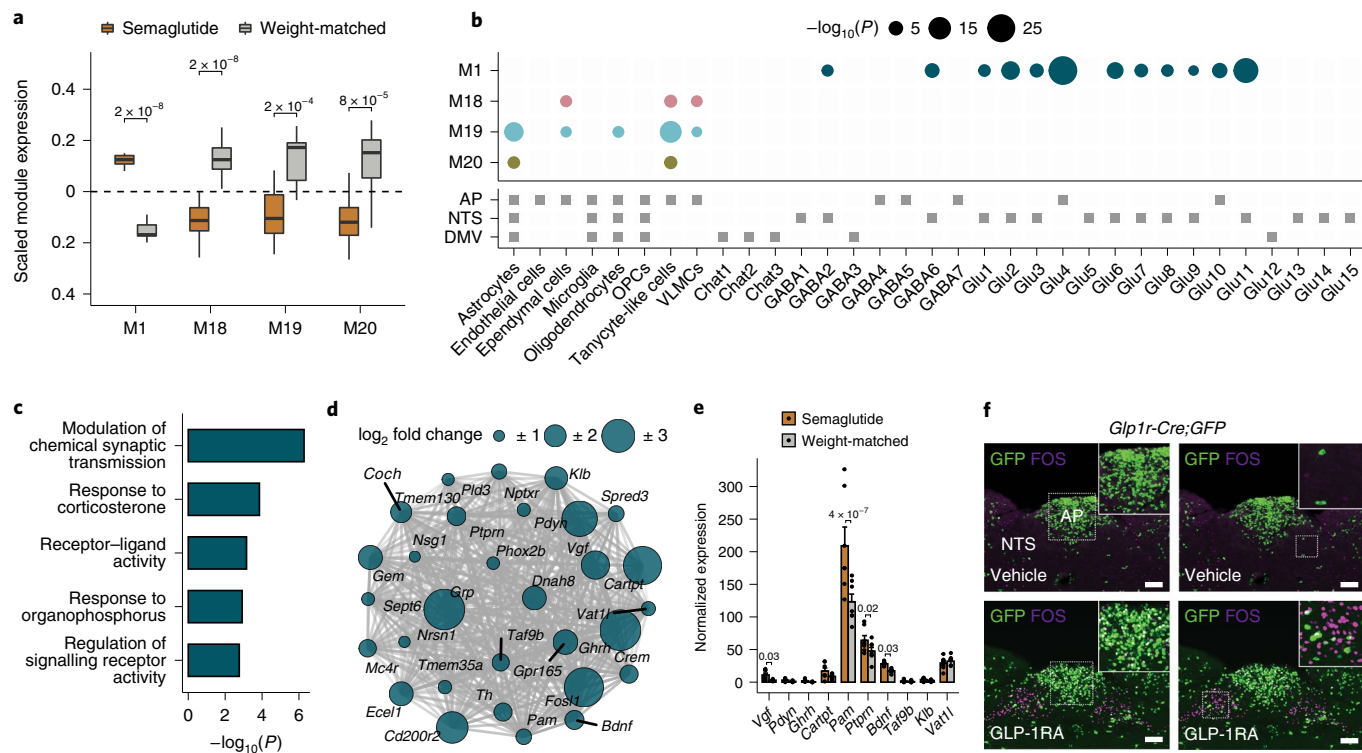


Fig. 4 | Transcriptional changes induced by GLP-1RA administration in glutamatergic *Glp1r* neurons. **a**, Modules correlated with GLP-1RA administration. Bulk RNA-seq data were clustered into modules of co-regulated genes. Data represent the median, and first and third quartiles and whiskers with minimum and maximum values represent 1.5 times the interquartile ranges. $P < 0.05$ are specified; semaglutide-administered ($n = 14$) versus weight-matched ($n = 13$) mice; logistic regression with Bonferroni-adjusted likelihood-ratio test. **b**, Cell population enrichment of module genes. Top, dot size indicates the significance level of overlap between module genes and cell population marker genes ($ES_\mu > 0$). Bonferroni-adjusted one-tailed Fisher's exact test. Bottom, the most likely DVC origin of the cell populations. **c**, Top five most enriched GO terms for module M1. Bonferroni-adjusted g:Profiler P value. **d**, Top 30 genes for module M1. Dot size indicates the log₂ fold change between semaglutide-treated and weight-matched animals. All genes were upregulated in the AP following semaglutide administration (BH-adjusted DESeq2 $P < 0.05$). **e**, Differential expression of the top ten M1 genes in Glu4^{AP} neurons. Values are the mean \pm s.e.m. $P < 0.05$ are specified; semaglutide-treated (784 neurons; $n = 7$) versus weight-matched (734 neurons; $n = 7$) mice; Bonferroni-adjusted pseudo-bulk DESeq2 P value. **f**, Representative images showing FOS immunoreactivity (purple) and GFP immunoreactivity (green) in *Glp1r-Cre;GFP* mice treated with Ex4 (i.p., 150 μ g kg⁻¹; $n = 3$) or vehicle ($n = 3$). Scale bar represents 150 μ m. i.p., intraperitoneal. Data for reconstruction of **d** are available in Supplementary Data 1 and 4 and/or at NCBI GEO.

positively and modules M18–20 negatively; Bonferroni-adjusted $P < 2.0 \times 10^{-4}$; Fig. 4a and Supplementary Data 4).

To assess whether these GLP-1RA-associated modules represented cell population-specific processes, we tested whether module genes selectively overlapped with cell population marker genes. The 581 genes in module M1 were broadly expressed in glutamatergic neurons and most strongly overlapped with Glu4^{AP} (*Glp1r/Gfral*) and Glu11^{NTS} (*Glp1r/Calcr*) neuronal marker genes (Bonferroni-adjusted $P < 7.2 \times 10^{-20}$), suggesting that these populations, but not GABA7^{AP} (*Glp1r*) neurons, respond directly to GLP-1RA administration (Fig. 4b). The 67 genes constituting module M18 overlapped with marker genes of ependymal cells, tanyocyte-like cells, and vascular and leptomeningeal cells (VLMCs); the 206 M19 genes were broadly expressed in glial cells; and the 143 M20 genes overlapped with marker genes of astrocytes and tanyocyte-like cells (Bonferroni-adjusted $P < 0.05$; Fig. 4b). These results demonstrate that GLP-1RA administration upregulates distinct biological processes in glutamatergic *Glp1r* neurons while decreasing transcriptional processes in glial cells.

To understand the transcriptional response to GLP-1RA administration in greater depth, we examined the enrichment of Gene Ontology (GO) biological processes and molecular functions in each module. We found that module M1 was most strongly associated with ‘modulation of chemical synaptic transmission’

(Bonferroni-adjusted $P = 5.3 \times 10^{-7}$; Fig. 4c), whereas M18 was most strongly associated with ‘calcium-dependent protein binding’, M19 with ‘rhythmic process’ and M20 with ‘negative regulation of neuron differentiation’ (Bonferroni-adjusted $P < 0.05$; Extended Data Fig. 7). Among the top genes in module M1 were *Bdnf*, *Mc4r*, *Vgf*, *Cartpt*, prohormone convertase 1 (*Pcsk1*) and *Th* (Fig. 4d and Supplementary Data 4). By applying db-ISH in mice treated with exendin-4 (Ex4; another GLP-1RA), we verified that *Bdnf* and *Mc4r*, which were undetectable in control mice, were upregulated in the AP after GLP-1RA administration (Extended Data Figs. 4e,g and 8). Finally, the top genes of module M1 were indeed upregulated after semaglutide administration in Glu4^{AP} (*Glp1r/Gfral*) neurons; four of these significantly, namely *Vgf*, peptidylglycine alpha-amidating monooxygenase (*Pam*), protein tyrosine phosphatase receptor type N (*Ptn*) and *Bdnf* (Bonferroni-adjusted $P < 0.05$; Fig. 4e). Together, these data suggest that GLP-1RA administration induces upregulation of neurotrophic and neuroendocrine genes in glutamatergic Glu4^{AP} (*Glp1r/Gfral*) neurons.

To further verify that *Glp1r* neurons in the AP and NTS are activated by GLP-1RA administration, we evaluated the expression of the activity-dependent immediate early gene FOS in *Glp1r-Cre* and *Calcr-Cre* mice before and after administration of Ex4. While GLP-1RA administration induced FOS immunoreactivity in *Glp1r* AP and NTS cells, a few *Calcr* AP cells were

positive for FOS after Ex4 administration (Fig. 4f and Extended Data Fig. 9a). As expected, an induction of FOS immunoreactivity in *Calcr* AP and NTS cells was seen after administration of sCT (Extended Data Fig. 9b). These results confirm selective activation of *Glp1r* AP and NTS neurons by GLP-1RAs.

Chromatin accessibility single-cell atlas of the dorsal vagal complex. To further characterize the regulatory landscape of DVC cells, we utilized snATAC-seq to profile chromatin accessibility in (1) semaglutide-administered, (2) ad libitum-fed vehicle-administered and (3) weight-matched control animals (from the same *in vivo* study as used for snRNA-seq data; Fig. 5a). The DNA fragment sizes of our snATAC-seq data displayed a classical decreasing distribution with peaks around 100 base pairs (bp), corresponding to nucleosome-free regions, and around 200 and 400 bp, corresponding to regions bound by mono- and di-nucleosomes, respectively (Fig. 5b). We retained 22,545 quality-filtered cells and identified neurons and the previously described eight glial cell types in similar proportions as those in the gene expression atlas (Spearman's rho = 0.92, $P = 0.001$; Fig. 5c). Likewise, all neuronal populations, except three populations (GABA^{7AP}, Glu14^{NTS} and Glu15^{NTS} neurons), were corroborated by snATAC-seq in comparable proportions (Spearman's rho = 0.91, $P = 3.7 \times 10^{-6}$; Fig. 5d). Thus, our single-nucleus chromatin accessibility data aligned well with our single-nucleus gene expression data.

We next investigated whether we could identify relevant cell population-specific transcription factor binding sites (henceforth 'motifs'). Across the glial cell types, we identified 174 enriched motifs (Bonferroni-adjusted $P < 0.05$; average of 45 motifs per cell population; Fig. 5e and Supplementary Data 5). There was a significant correlation between the motif enrichment and the expression specificity of the corresponding transcription factor (median Spearman's rho = 0.21; $P = 1.1 \times 10^{-23}$), suggesting our data allows for identification of relevant cell population-specific accessible motifs. Across the neuronal populations, we identified 315 enriched motifs (Bonferroni-adjusted $P < 0.05$; average of 45 enriched motifs per neuronal population; Fig. 5f and Supplementary Data 5). We again observed a correlation between motif enrichment and transcription factor expression specificity (median Spearman correlation = 0.11, Fisher's exact test $P = 8.5 \times 10^{-26}$). There was a high similarity between neurons of the same neurotransmitter class at the motif level (see dendrogram in Fig. 5f). Among the most enriched motifs in Glu4^{AP} (*Glp1r/Gfral*) and Glu11^{NTS} (*Glp1r/Calcr*) neurons were PHOX2A and PHOX2B, which are involved in the transcription of *Dbh*, consistent with the noradrenergic profile of these neurons³².

Finally, we assessed whether GLP-1RA administration induced changes at the chromatin level. Since 16 genes in the semaglutide-associated module M1 encode transcription factors, we next asked whether the corresponding motifs were enriched in Glu4^{AP} (*Glp1r/Gfral*) neurons from semaglutide-administered animals. Fifteen of 16 motifs displayed enriched accessibility after GLP-1RA administration, of which eight remained significant after multiple-testing correction (Bonferroni-adjusted $P < 0.05$; Fig. 5g). Four of these motifs (FOS, FOSL1, FOSL2 and JUNB) can be bound by stimulus-induced early-response gene transcription factors³³. These results reinforce the above observations that Glu4^{AP} (*Glp1r/Gfral*) neurons are activated by GLP-1RA administration.

Assessing relevance in humans using genetic data. To assess the extent to which DVC cell populations are likely to impact genetic susceptibility to obesity, we integrated our single-cell atlases with GWAS data for BMI. Specifically, we asked whether human orthologues of genes marking DVC cell populations nonrandomly colocalized with genetic variants associated with BMI. We subsequently validated these findings by testing whether regions of accessible chromatin with cell population-specific motifs also preferentially colocalized with BMI-associated genetic variants (Fig. 6a).

By applying CELLECT⁷ to address these questions, we identified four cell populations, exclusively glutamatergic neurons, comprising marker genes colocalizing with BMI-associated genetic variants (Bonferroni-adjusted $P < 0.05$; Fig. 6b). Glu10^{AP} (*Calcr/Ramp3*) neurons displayed the strongest enrichment, implicating a role for amylin-sensing AP neurons in body weight control. Glu9^{NTS} neurons (top marker gene, *Eya1*) displayed the second strongest enrichment. Finally, we also detected enrichments for Glu4^{AP} (*Glp1r/Gfral*) and Glu11^{NTS} (*Glp1r/Calcr*) neurons. These results suggest that *Calcr*- and/or *Glp1r*-expressing AP and NTS neurons may contribute to the genetic control of body weight.

Integration of the BMI GWAS data with the chromatin accessibility data supported the above results (Spearman's rho = 0.8, $P = 1.3 \times 10^{-6}$); five exclusively glutamatergic neuronal populations comprised accessible motifs near BMI-associated genetic variants (Bonferroni-adjusted $P < 0.05$; Fig. 6c). Again, Glu10^{AP} (*Calcr/Ramp3*) neurons displayed the strongest enrichment, thus establishing that both the gene expression and chromatin accessibility profiles of these neurons position them as likely regulators of susceptibility to obesity. While Glu4^{AP} (*Glp1r/Gfral*) and Glu11^{NTS} (*Glp1r/Calcr*) neurons were nominally enriched, these results did not withstand adjustment for multiple testing (non-adjusted $P = 1.7 \times 10^{-3}$ and $P = 4.7 \times 10^{-3}$, respectively).

We conducted a meta-analysis on the results from the integration of BMI GWAS data with gene expression and chromatin accessibility data. Top-ranking cell populations mediating genetic susceptibility to obesity were: (1) Glu10^{AP} (*Calcr/Ramp3*), (2) Glu9^{NTS} (*Eya1*), (3) Glu4^{AP} (*Glp1r/Gfral*) and (4) Glu11^{NTS} (*Glp1r/Calcr*) neurons (Bonferroni-adjusted $P < 3.0 \times 10^{-3}$; Supplementary Data 6). Together, these results imply a physiological role of AP and NTS glutamatergic neurons, especially those that express *Calcr* and/or *Glp1r*, in the control of food intake and body weight, consistent with the capabilities of pharmacological GLP-1RA and CALCR agonist administration to reduce body weight. These results are also consistent with previous findings¹⁷ and our observation that activation of *Calcr* NTS neurons suppresses food intake and body weight (Extended Data Fig. 10).

We next tested the predicted role of Glu10^{AP} (*Calcr/Ramp3*) neurons in the control of food intake. Because stereotaxic manipulation of AP neurons in mice is difficult, we used CRISPR-Cas9 genome engineering to generate a *Calcr-Cre* knock-in rat model (Fig. 6d and Supplementary Fig. 1). We injected AAV-hM3Dq-mCherry, which expresses the activating hM3Dq designer receptor exclusively activated by designer drugs (DREADD) in a Cre-inducible manner, into the AP of *Calcr-Cre* rats and confirmed that DREADD expression was specific to the AP (Fig. 6e and Supplementary Fig. 2). We then examined food intake over 24 h in these rats following injection of saline or clozapine-N-oxide (CNO), which activates hM3Dq, and found that DREADD-mediated activation of *Calcr* AP neurons in rats durably decreased food intake, consistent with a role for Glu10^{AP} (*Calcr/Ramp3*) neurons in the control of feeding (Fig. 6f). Importantly, CNO injection in *Calcr-Cre* rats without DREADD expression did not alter feeding (Fig. 6g). The observed anorexic effects following activation of *Calcr* AP and NTS neurons reinforce their potential utility as targets for therapeutic intervention in obesity.

Discussion

Here we investigated the contribution of DVC cell populations in the pharmacological and physiological control of energy balance. By applying snRNA-seq and snATAC-seq, we identified eight non-neuronal and 25 neuronal populations with distinct gene expression and motif accessibility landscapes. By combining our single-cell atlases with bulk RNA-seq, we show that GLP-1RA-induced alterations in gene expression and chromatin accessibility are specific to AP neurons that express *Glp1r* and *Gfral* and NTS neurons that

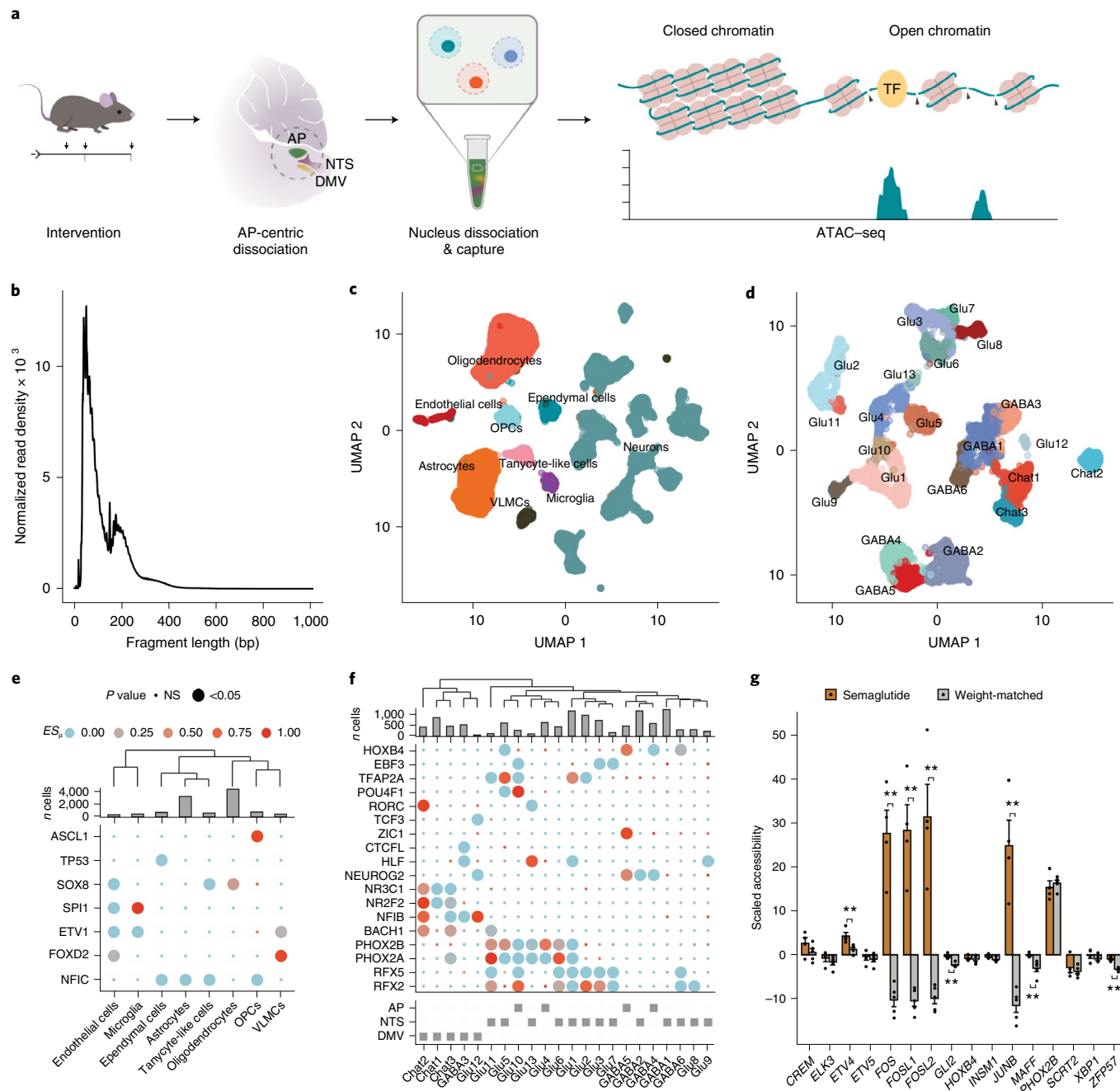


Fig. 5 | Chromatin accessibility atlas of DVC cell populations. **a**, Overview of snATAC-seq study design. DIO mice were randomized into three groups: semaglutide-administered ($n=5$), ad libitum-fed vehicle-administered ($n=5$) and weight-matched control ($n=5$) mice that were dosed once daily for 7 d (same in vivo study as for the snRNA-seq data). The AP, NTS and DMV were dissociated and subjected to snATAC-seq. **b**, Fragment size distribution for snATAC-seq data. **c**, UMAP plot of the 22,545 cells coloured by cell type. **d**, UMAP plot of the 11,651 neurons coloured by population. **e**, Motif enrichment in non-neuronal cells. From top to bottom: dendrogram showing the cell type similarity in motif accessibility, number of cells per cluster and most enriched motifs coloured by the expression specificity values (ES_μ) of the corresponding transcription factor genes. Enriched motifs were identified using logistic regression with Bonferroni-adjusted likelihood-ratio test. **f**, Motif enrichment in neuronal populations. From top to bottom: dendrogram showing the neuronal population similarity in motif accessibility, number of cells per cluster, the most enriched motifs coloured by the ES_μ values of the corresponding transcription factor genes and the most likely DVC origin of the neuronal populations. **g**, Differential motif accessibility in Glu4^{AP} neurons for GLP-1RA-induced transcription factors. Values are the mean \pm s.e.m. ** $P=0.007$; semaglutide (182 neurons, $n=5$ mice) versus weight-matched (239 neurons, $n=5$ mice); pseudo-bulk logistic regression with Bonferroni-adjusted likelihood-ratio test. NS, not significant. Data for reconstruction of **b–f** are available in Supplementary Data 5 and at NCBI GEO.

express *Glp1r* and *Calcr*. These neuronal populations, along with AP neurons that express *Calcr* and *Ramp3*, exhibit marker genes and accessible motifs colocalizing with BMI-associated genetic variants.

Furthermore, using a new *Calcr-Cre* rat model, we show that activation of *Calcr* AP neurons suppresses food intake. Together, these findings implicate *Glp1r/Gfral* AP neurons, *Glp1r/Calcr* NTS

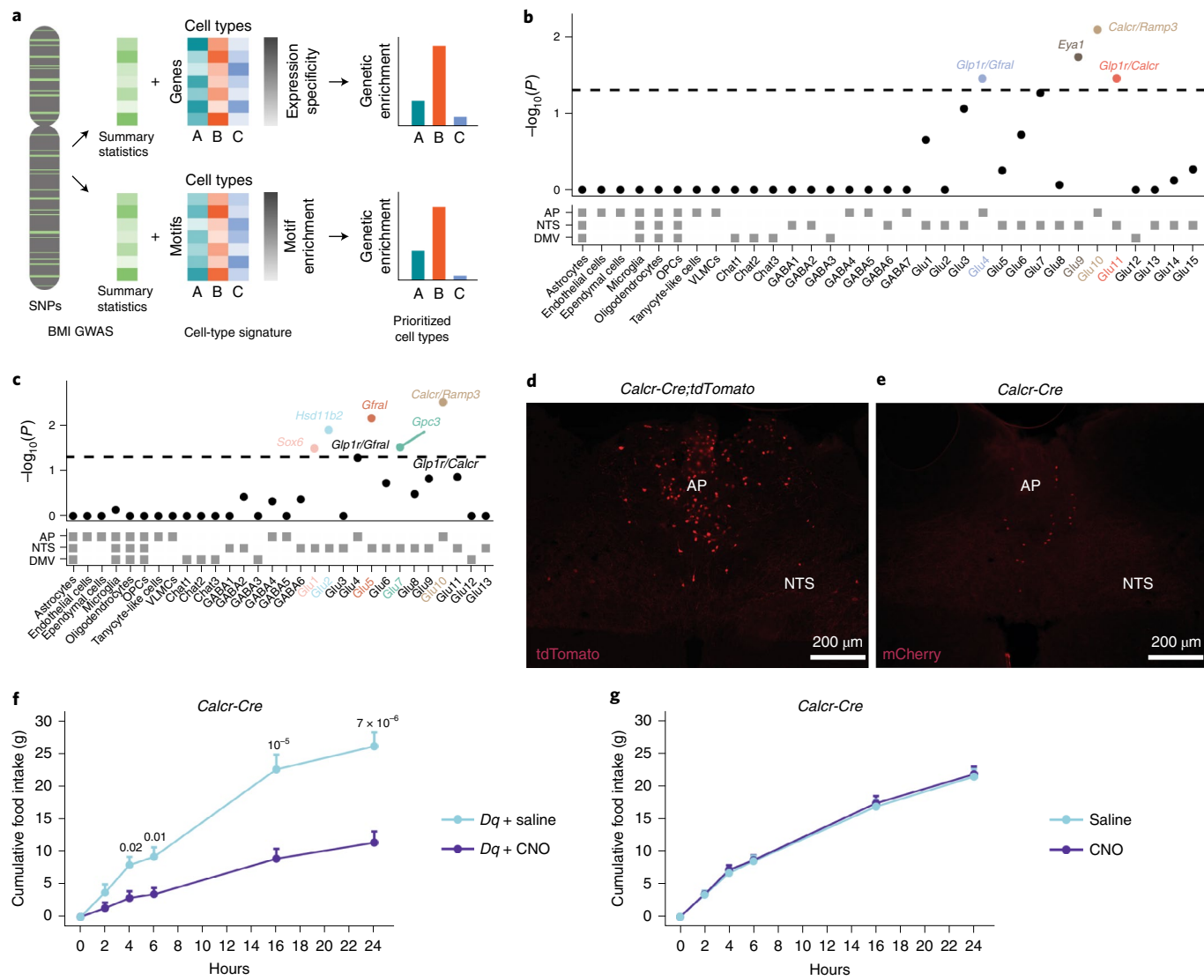


Fig. 6 | *Glp1r* and *Calcr* neurons enrich for genetic variants associated with BMI. **a**, Overview of BMI GWAS integration. The expression specificity profile (top) or the motif enrichment (bottom) for each cell population was integrated with BMI GWAS data to compute the genetic enrichment in each cell population. **b,c**, BMI GWAS integration with gene expression (**b**) and motif accessibility (**c**). Top, genetic enrichment. Bonferroni-adjusted CELLECT *P* value. The dashed line indicates the significance threshold. Bottom, the most likely DVC origin of the neuronal populations. **d**, Representative image showing tdTomato immunoreactivity (red) in *Calcr-Cre*;tdTomato reporter rats ($n=5$). **e**, Representative image showing mCherry immunoreactivity (red) in *Calcr-Cre* rats injected with hM3Dq-mCherry in the AP ($n=4$). Scale bars for **d** and **e** represent 200 μ m. **f**, Food intake in *Calcr-Cre* rats injected with hM3Dq-mCherry in the AP following treatment with saline ($n=4$) or CNO (i.p., 1 mg kg $^{-1}$; $n=4$). **g**, Food intake in *Calcr-Cre* rats following treatment with saline ($n=10$) or CNO (i.p., 1 mg kg $^{-1}$; $n=10$). Values are the mean \pm s.e.m. $P < 0.05$ are specified, linear mixed-effects model; least-squares means with Bonferroni-adjusted two-tailed *t*-test. SNP, single-nucleotide polymorphism.

neurons and *Calcr/Ramp3* AP neurons in the genetic predisposition to obesity and suggest that these cell populations represent relevant therapeutic targets for obesity.

Several of the 33 cell populations identified here align well with previous observations. First, we report an overrepresentation of glutamatergic (Glu1–15) neurons in the AP and NTS²⁴. Second, we identified a partial overlap between *Glp1r* and *Gfral* (Glu4) neurons exclusively in the AP³⁴. Third, we report a noradrenergic phenotype of *Glp1r* (Glu4 and Glu11) neurons in the AP and NTS^{10,28}. Fourth, we detected a population of *Calcr* (Glu10) neurons coexpressing *Ramp3* in the AP³⁵. Finally, we identified distinct glial cell types with previously characterized marker genes. Among these populations, VLMCs, ependymal cells and endothelial cells were more strongly

enriched in the AP in the DVC consistent with increased vascularization of circumventricular organs³⁶. We extend these findings by showing that: (1) there exists a subset of neurons (Glu11) containing *Glp1r* and *Calcr* in the NTS; (2) *Gipr* is expressed in GABAergic (GABA5) neurons in the AP; and (3) *Casr*, *Grpr*, *Olf78* and *Pax5* mark *Glp1r* (Glu4) AP, *Glp1r/Calcr* (Glu11) NTS, *Calcr* (Glu10) AP and *Gipr* (GABA5) AP neurons, respectively. During the revision phase of this paper, a single-nucleus gene expression atlas focused on nausea-promoting cells of the AP was published³⁷. The AP- and nausea-focused study supports a number of findings reported here, the two most important being that distinct glutamatergic neuronal populations in the AP express *Glp1r*, *Gfral* and *Casr* (Glu4), while others express *Calcr*, *Ramp3* and *Olf78* (Glu10), and that *Gipr* is

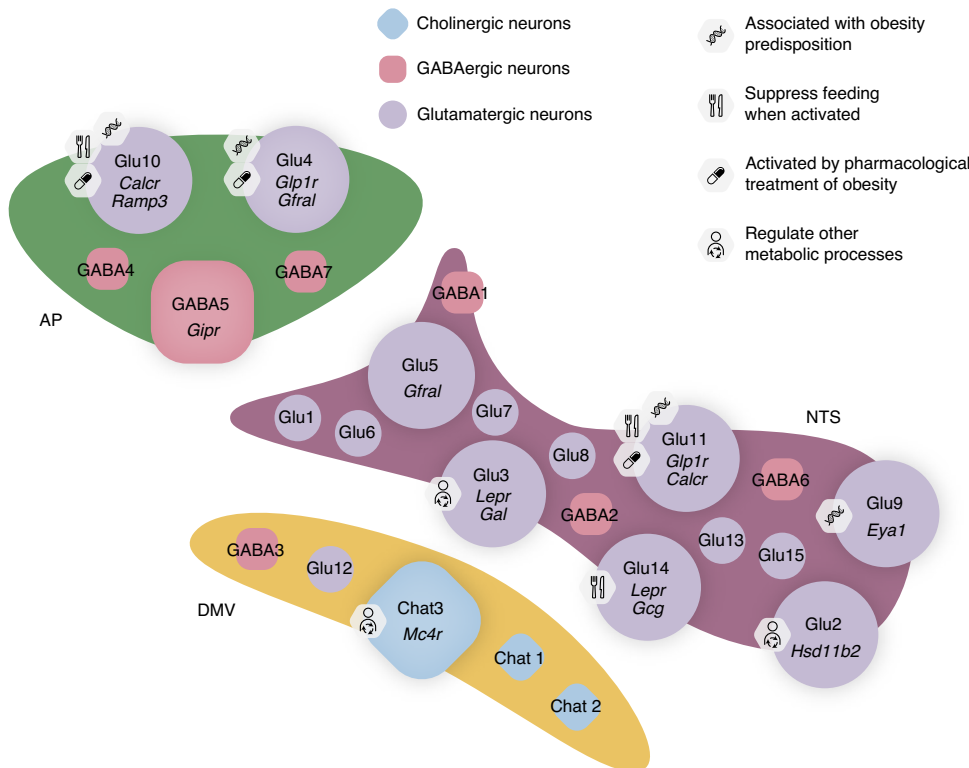


Fig. 7 | Overview of DVC neuronal populations and their role in metabolism. Single-nucleus RNA-seq profiling of 49,392 neurons in the DVC identified a total of 25 neuronal populations distributed across the AP ($n=5$), NTS ($n=15$) and DMV ($n=5$). Integrating the single-cell data with GWAS data for BMI showed that Glu4^{AP}, Glu9^{NTS}, Glu10^{AP} and Glu11^{NTS} neurons expressed marker genes with human orthologues that nonrandomly colocalized with BMI-associated genetic variants. Glu10^{AP}, Glu11^{NTS} and Glu14^{NTS} neurons (refs. ^{30,38}) suppress feeding when activated by DREADDs. Glu4^{AP} neurons are activated by GLP-1RAs, Glu10^{AP} neurons by sCT and Glu11^{NTS} neurons by GLP-1RAs and sCT. Chat3^{DMV} neurons regulate circulating insulin³⁹, Glu2^{NTS} neurons drive sodium appetite⁴⁰ and Glu3^{NTS} neurons modulate breathing via leptin-mediated mechanisms⁴¹. We note that functions for other DVC populations remain to be determined. Within each of the three DVC nuclei, the spatial placement of the neuronal populations is arbitrary. Magnified neuronal shapes denote neuronal populations with genetic enrichments, potential or proven utility as targets for therapeutic intervention in obesity, or roles in central regulation of feeding or other metabolic processes. Shapes and colours indicate neurotransmitter type (circle, glutamatergic; square, GABAergic; diamond, cholinergic).

expressed by GABAergic (GABA5) AP neurons. In addition to *Eya1* (Glu9) NTS neurons that represent candidates for the control of energy balance, other cell populations identified in our atlas with relevance to metabolism include *Gfral* (Glu5) NTS neurons, *Lepr/Gcg* (Glu14) NTS neurons that suppress feeding^{30,38}, *Mc4r* (Chat3) DMV neurons that are involved in insulin regulation³⁹, *Hsd11b2* (Glu2) NTS neurons that drive sodium appetite⁴⁰ and *Lepr/Gal* (Glu3) NTS neurons that modulate respiration⁴¹ (Fig. 7). These consistencies in DVC cell population identities with previous studies and our non-human primate db-ISH data further position our transcriptional and chromatin accessibility single-cell atlases as valuable resources for future studies directed towards the DVC.

Among the six brain areas transcriptionally characterized in our work, GLP-1RA administration induced the strongest transcriptional changes in the AP. We did not identify major differences between semaglutide and liraglutide administration, suggesting that the superior weight-lowering effects of semaglutide is mediated through brain areas or mechanisms not covered by our analyses. Genes upregulated following semaglutide administration (captured in module M1) were specifically expressed in glutamatergic *Glp1r/Gfral* (Glu4) AP and *Glp1r/Calcr* (Glu11) NTS neurons, supporting a role for glutamatergic neurons in GLP-1RA-induced weight loss²⁴ and aligning with observations that NTS intraparenchymal delivery of GLP-1RA suppresses food intake^{15,16}. These genes were not specific to *Gcg* (Glu14) neurons in the NTS, consistent with previous observations showing that GLP-1RAs have

anorexic effects independently of *Gcg* NTS neurons, and that these neurons have limited interactions with AP neurons and vice versa^{30,42}. Top genes of the GLP-1RA-induced response included *Bdnf*, *Mc4r* and *Pcsk1*. Several of these genes have established roles in body weight control including: (1) protein-altering mutations and deletions in *BDNF*, *MC4R* and *PCSK1* can cause early-onset severe obesity in humans^{43,44}, (2) DVC intraparenchymal infusion of BDNF and MC4R agonists both reduce food intake and body weight^{45,46}, and (3) body weight suppressive effects of GLP-1RA administration is attenuated with DVC intraparenchymal infusion of an MC4R antagonist, suggesting that GLP-1RA stimulation depends on MC4R activation by endogenous ligands such as α -melanocyte-stimulating hormone⁴⁷.

A key strength of our approach is that we can implicate cell populations with relevance to human obesity by matching hundreds of genetic loci associated with BMI to the gene regulatory signatures of DVC cell populations. Our data-driven approach associated four neuronal populations with genetic obesity predisposition (Glu4, Glu9, Glu10 and Glu11), three of which carry pharmacological relevance by expressing *Glp1r* and/or *Calcr*. These findings indicate their long-term weight-regulatory relevance, and indeed, knockout of *Calcr* in the AP and NTS blunts the anorexic effects of amylin¹⁸, while both *Glp1r* NTS knockout and intraparenchymal delivery of exendin-9 (a GLP-1R antagonist) increases food intake^{48,49}. Furthermore, knockout of *Calcr* in the NTS attenuates the anorexic effects of sCT, while *Calcr* neurons in the AP may also contribute

to the sCT response because AP lesions blunt both amylin- and sCT-mediated suppression of food intake¹⁴. Our findings further establish the importance of *Calcr* (Glu10 and Glu11) neurons in the DVC and show that activation of both *Calcr* AP and *Calcr* NTS neurons decreases food intake. In contrast to *Calcr* NTS neurons, the vast majority of *Calcr* AP neurons did not express *Glp1r*; however, additional experiments are needed to fully rule out the possibility that *Glp1r* neurons contribute to the *Calcr* AP-mediated feeding suppression. We additionally report a previously uncharacterized population of *Eya1* (Glu9) NTS neurons are associated with susceptibility to obesity. The exact role of these neurons in body weight control will have to be addressed in future studies.

Nausea, an unpleasant feeling of visceral malaise, represents an important therapy-limiting side effect of previous drug candidates targeting the AP⁵⁰. Hence a key question remains whether any of the likely body-weight-regulatory DVC neuronal populations induce nausea. Notably, *Calcr* AP and *Calcr* NTS neurons do not promote conditioned taste aversion in mice (a response that can be indicative of nausea)^{17,37}. In contrast, activation of *Glp1r* AP and *Gfral* AP neurons induces conditioned taste aversion³⁷. Due to the colocalization of *Calcr* and *Glp1r* in the NTS and the non-aversive nature of *Calcr* NTS neurons¹⁷, it seems less likely that *Glp1r* NTS neurons are aversive. The findings in rodents are partly contradicted by phase III clinical trial data in patients with type 2 diabetes, showing that semaglutide-induced weight loss can only to a minor extent be explained by nausea or vomiting⁵¹. Thus, whereas at least activation of rodent *Glp1r* AP neurons may lead to nausea, the feeding response driven by activation of *Calcr* AP neurons (the cell population most strongly enriched for genes colocalizing with BMI GWAS variants) is less likely to be caused by nausea. However, the present study does not fully eliminate aversion as a possible mechanism of reduced feeding.

Despite its strengths, our study has a number of limitations. First, there were slight differences between the two *in vivo* studies performed here; semaglutide-administered mice weighed approximately 1 g less than their weight-matched controls in the snRNA-seq- and snATAC-seq-focused *in vivo* study, whereby the difference in food intake was not as significant as in the bulk RNA-seq-focused study. Second, due to a typically relatively low mRNA capture rate in the droplet-based single-cell techniques, we cannot rule out that additional relevant genes are expressed in the cell populations characterized here. For instance, although α-melanocyte-stimulating hormone is a proopiomelanocortin (POMC)-derived peptide reported to be expressed in the ARH and NTS⁵², we were not able to identify *Pomc* NTS neurons in our DVC atlas. Third, although our results imply a role for *Glp1r* AP neurons as key mediators of GLP-1RA-induced weight loss, other studies have shown that the AP may not be required for these anorectic effects^{37,53,54}. This apparent contradiction may be explained by the expression of *Glp1r* in the NTS and elsewhere in the brain and by the access of long-acting GLP-1RAs to several sites contributing to the efficacy of GLP-1RA administration²⁵. Finally, the genetic enrichment analysis relies on the assumption that gene expression levels and chromatin accessibility are relatively conserved between the mouse and human species.

In conclusion, our results suggest that *Glp1r* and *Calcr* neurons in the AP and NTS represent therapeutic targets that express genes and contain accessible DNA sequence motifs with likely roles in predisposition to obesity in humans, and our single-cell transcriptomics and chromatin accessibility atlases constitute comprehensive molecular resources for further exploration of DVC cells in obesity and beyond.

Methods

Bulk and single-nucleus RNA-seq and ATAC-seq. Mice. All *in vivo* experiments were conducted in accordance with internationally accepted principles for the

care and use of laboratory animals approved by the Danish Ethical Committee for Animal Research.

For the bulk RNA-seq experiment, 7-week-old C57BL/6 male mice were obtained from JanVier Labs. On arrival to the animal unit, mice were group housed (ten animals per cage) with ad libitum access to a 60% HFD (12492, Research Diets) and tap water. Animals were fed the HFD for at least 24 weeks before study start to ensure DIO. The animal room environment was controlled (temperature 22 ± 2 °C; relative humidity 50% ± 10%; 12-h light/dark cycle).

For the snRNA-seq experiment, 20-week-old DIO (16 weeks of HFD) male C57BL/6 mice were obtained from Charles River. On arrival to the animal unit, mice were single housed with ad libitum access to a 60% HFD (12492, Research Diets) and tap water for 6 weeks before study start. The animals were housed as described above.

Randomization and dosing. For the bulk RNA-seq experiment, 2 weeks before study onset, animals were single housed and their daily food intake was recorded for the last 6 d before study start. On the day before study onset, animals were block randomized based on body weight into the following groups: (1) semaglutide-administered ($n = 15$), (2) liraglutide-administered ($n = 15$), (3) vehicle-administered and ad libitum-fed ($n = 15$) and (4) vehicle-administered and weight-matched to the semaglutide group ($n = 15$). For each group, animals were divided into two subgroups where dosing was initiated with a 1-d interval. Animals were dosed subcutaneously once daily, for 7 d approximately 3 h before lights off. Dosing of the animals was gradually up-titrated with the following daily increments to avoid initial discomfort and potential dehydration: 0.02, 0.04 and 0.1 mg kg⁻¹ for semaglutide and 0.2, 0.4 and 1.0 mg kg⁻¹ for liraglutide. Animals were terminated by decapitation under CO₂/O₂ anaesthesia the day after the last dose. All animals were terminated in 3–4 h after lights on in the morning of the day after the last dose, to ensure minimal variation in gene expression caused by circadian rhythm.

Unless otherwise specified, the above experimental set-up was replicated for the *in vivo* study used to generate the snRNA-seq and snATAC-seq data. On the day before study start, animals were block randomized based on body weight into the following groups: (1) semaglutide-administered ($n = 9$; snRNA-seq, $n = 4$; snATAC-seq, $n = 2$; snRNA-seq and snATAC-seq, $n = 3$), (2) vehicle-administered and ad libitum-fed ($n = 9$; snRNA-seq, $n = 4$; snATAC-seq, $n = 3$; snRNA-seq and snATAC-seq, $n = 2$) and (3) weight-matched to the semaglutide group ($n = 8$; snRNA-seq, $n = 3$; snATAC-seq, $n = 1$; snRNA-seq and snATAC-seq, $n = 4$). Please refer to the Reporting Summary for additional information on the *in vivo* studies and related experiments.

Generation of bulk RNA-seq data. After decapitation, brains were stored at -80 °C until further processing. The frozen brains were slightly thawed to -20 °C and divided into three parts (forebrain, midbrain and hindbrain) by two dorsoventral cuts at the optic chiasm and just rostral to the cerebellum. Each part of the brain was cut on a cryostat (CM3050S, Leica) into 12-mm thick coronal sections, and serial sections were collected on Arcturus PEN membrane slides (Applied Biosystems). Slides were stored at -80 °C until laser capture microscopy. Sectioning was optimized for each region to ensure a sufficient RNA (approximately 30 ng) for the sequencing process; LS, bregma 0.74 to 0.14 mm; PVH, bregma -0.58 to -1.22 mm; ARH, bregma -1.46 to -2.18 mm; DMH, bregma -1.58 to -2.18 mm; NTS, bregma -7.20 mm to end of NTS; AP, bregma -7.20 mm to end of AP. Following laser capture microscopy, RNA extraction was performed using the PicoPure RNA Isolation Kit (Applied Biosystems) as recommended by manufacturer, including an Ambion DNase treatment (Invitrogen).

Generation of AP-centric DVC single-nucleus suspensions. After decapitation, the brains were excised, and the AP-centric DVCs were directly removed from the brainstem by dissection and stored at -80 °C. Nuclei were purified with reagents from the Nuclei Pure Prep Nuclei Isolation Kit (Sigma-Aldrich, NUC-201). Lysis buffer (LB) and 1.8 M sucrose cushion (SC) solution was prepared as recommended by the manufacturer, with the addition of 80 U Protector RNase Inhibitor (Sigma-Aldrich, 33353399001) per ml of LB. All reagents and samples were kept cold on wet ice throughout the process. Samples were thawed on ice for 1 min and homogenized in 10–20 µl LB by pipetting up and down until the tissue appeared thoroughly degraded. Then LB was added to a total of 50 µl, and the homogenate was gently laid on top of two pre-vetted filters (a pluriStrainer Mini 40 µm on top of a pluriStrainer Mini 20 µm (pluriSelect)). The filters were rinsed with 2 × 200 µl LB followed by 2 × 500 µl SC. The top filter was discarded, and the sample and the remaining filter was spun for 30 s at 290g. The filtered sample was mixed by pipetting and carefully laid on top of 500 µl SC and spun for 10 min at 10,000g at 4 °C. The top layer was removed, leaving ~500 µl of sample with the pellet. PBS-BSA (PBS with 1% BSA, sterile filtered) was added to a total of 2 ml, the sample was mixed by pipetting and spun for 5 min at 500g at 4 °C. The supernatant was carefully removed, leaving ~100 µl of sample with the pellet, and the PBS-BSA wash was repeated. Following the final spin, ~100 µl of sample was left after removal of supernatant, and the pelleted nuclei were resuspended in this remaining sample buffer. The nuclei concentration was measured, and 9,000 nuclei were used for snRNA-seq and snATAC-seq.

Bulk RNA-seq library preparation. From the extracted RNA, stranded mRNA libraries were produced using the TruSeq Stranded mRNA Kit (Illumina), followed by sequencing of single-end, 75-bp reads on a NextSeq 500 platform (Illumina) to a depth of approximately 1.5×10^7 reads per sample.

Single-nucleus RNA-seq and ATAC-seq library preparation. Libraries for snRNA-seq and snATAC-seq were prepared using the 10x Genomics Chromium single-cell 3' reagent kits (version 2) and Chromium single-cell ATAC reagent kits as recommended by the manufacturer. Libraries were sequenced on an Illumina NovaSeq 6000 and a NextSeq 500 sequencing system to a depth of approximately 2.3×10^8 and 7×10^7 reads per sample for the snRNA-seq and snATAC-seq libraries, respectively.

In vivo study data statistical analyses. Statistical analyses on mouse in vivo study data were performed using a linear mixed-effects model with food intake or body weight as the dependent variable, treatment group and time point as independent variables with interaction effects, and mouse as the random effect. Group contrasts were tested using a least-squares means two-tailed *t*-test, and *P* values were adjusted for multiple testing using the Bonferroni method.

Bulk and single-nucleus RNA-sequencing data analysis. **Bulk RNA-sequencing raw data processing.** Base calling and demultiplexing was performed with Illumina bcl2fastq version 2.17.1.14. The sequencing data were aligned to the *Mus musculus* (mm10) genome using STAR version 2.5.2a with default parameters. STAR was also used for feature counting. Quantification and identification of differentially expressed genes (Supplementary Data 1) were carried out using DESeq2 (ref. 55), and *P* values were adjusted for multiple testing using the Bonferroni method.

Re-annotation of the *Glp1r* genomic coordinates. The PolyA_DB database⁵⁶ version 3.2 was used to identify genomic coordinates for alternative poly(A) sites in the *Glp1r* and *Ghsr* genes. UCSC liftOver⁵⁷ was used to convert the coordinates from the genome build mm9 to mm10. The transcription end coordinates for *Glp1r* and *Ghsr* were re-annotated to be the most downstream poly(A) sites.

Single-nucleus RNA-sequencing raw data processing and quality control. Raw sequencing reads were processed using the 10x Genomics Cell Ranger version 3.0 pipeline and aligned to the *Mus musculus* (mm10) genome with default parameters. For each sample, a unique molecular identifier count matrix was generated using both exonic and intronic reads. Normalization, alignment and dimensionality reduction were performed using Seurat⁵⁸ version 3.1.1. Cells with a mitochondrial RNA content of >5% were discarded ($n=2,003$), and doublets were removed ($n=2,815$) using DoubletFinder⁵⁹ version 2.0.0. Counts for each cell were normalized by the total gene expression of that cell, multiplied by 10,000, and log transformed. To remove variance attributed to batch for downstream visualization and clustering, samples were integrated using the 'FindIntegrationAnchors' and 'IntegrateData' Seurat functions, which use canonical correlation analysis followed by mutual nearest-neighbourhood detection to align cells across samples. The integrated dataset was centred and scaled, PCA was carried out, and the top 30 PCs were used as input for UMAP dimensionality reduction. The above quality controls reduced our snRNA-seq dataset from 82,413 to 77,605 cells.

Single-nucleus RNA-sequencing cell population identification. Cell clustering was carried out on the integrated dataset using the Seurat functions 'FindNeighbors' and 'FindClusters' using Louvain community detection. Major cell populations were separated by an initial round of clustering and classified based on the expression of known marker genes (a resolution of 0.3 was chosen based on the best visual separation of non-neuronal cell clusters). Mapping of microglia and tanyocyte-like cells between the present and the published ARH-ME dataset²² was performed by projecting the ARH-ME dataset PCA structure onto the present dataset followed by mutual nearest-neighbourhood detection using the Seurat functions 'FindTransferAnchors' and 'TransferData' (confidence score > 0.5). For each cell, the silhouette index, a measure quantifying the similarity of a given cell to its assigned cluster compared to other clusters, was computed. Subsequently, to remove cells that could not confidently be assigned to a single cluster, cells with a negative silhouette index were discarded ($n=1,822$).

After these quality-control steps, it was evident that a few cells labelled as astrocytes, oligodendrocytes and microglia were most similar to other cell populations than their assigned ones in UMAP space. To remove likely missed doublets, all genes across all cells were clustered into modules of coexpressed genes using WGCNA⁶⁰. Cells that were not annotated as oligodendrocytes or OPCs and that had high loading (module eigengene > 5% quantile of oligodendrocytes) on the oligodendrocyte-specific module were removed. Likewise, cells that were not astrocytes, VLMCs, tanyocyte-like cells, endothelial cells or ependymal cells and loaded high on the astrocyte-specific module were removed, as were non-microglial cells that loaded high on the microglia-specific module. During this filtering step, 758 cells were discarded.

Finally, to identify robust neuronal populations, we applied the following two-step procedure. First, neurons ($n=52,289$) were clustered at ten different low resolutions (0.01–0.1), and the run with the highest average silhouette index

was chosen (resolution of 0.1; 11 clusters). Cells that could not be confidently assigned to a major neuronal class were discarded (cells with negative silhouette indices were removed). Second, neurons (mean silhouette index, 0.31; median silhouette index, 0.30) were subclustered in a more fine-grained manner by testing 100 different resolutions varying from 0.01 to 1. Each run was scored by the silhouette index, and the run exhibiting the highest average silhouette index was chosen for all downstream analyses (resolution of 0.44; 25 clusters; mean silhouette index, 0.34; median silhouette index, 0.36). This final filtering step removed 2,897 neuronal cells, leaving 49,392 neuronal and 22,736 non-neuronal cells for the downstream analyses (72,128 in total). The mean and median number of transcripts recovered per cell were 2,093 and 1,354, respectively, and the mean and median number of unique genes recovered were 1,112 and 876, respectively.

Expression specificity. Cell population marker genes were identified with CELLEX version 1.1.1 (<https://github.com/perslab/CELLEX/>) using default parameters. For glial cell types, the gene with the highest CELLEX score that was also a marker of the corresponding glial cell type in the hypothalamus^{22,61,62} was depicted. For neuronal cell populations, the gene with the highest CELLEX score that was expressed in >10% of cells of the corresponding cell population was reported.

Enrichment of the area postrema and nucleus of the solitary tract markers. Differentially expressed genes between the bulk RNA-seq AP and NTS samples (Supplementary Data 3) were identified using DESeq2, and *P* values were adjusted for multiple testing using the BH method. AP and NTS markers were ranked by *P* values, and cell population marker genes ($ES_{\mu} > 0$) were tested for the enrichment of the top 1,000 marker genes for the AP and NTS, using a one-tailed Fisher's exact test. *P* values were adjusted for multiple testing using the Bonferroni method (adjusting for the number of cell populations × number of brain areas).

Weighted gene coexpression network analysis. WGCNA was run using the R implementation. The bulk RNA-seq data were subject to variance stabilizing transformation normalization using DESeq2, and genes with a variance of zero were removed. Using the biweight midcorrelation, a similarity matrix was computed from which a signed network was constructed using a soft-thresholding power of five, maximizing the scale-free topology R^2 fit. Genes were clustered hierarchically based on the average topological overlap measure, and modules of coexpressed genes were identified using the 'cutreeDynamic' function with the parameters 'minClusterSize' set to 30, 'deepSplit' set to three and 'pamStage' set to false. Finally, the Pearson correlation between the module eigengenes was computed, and modules with a correlation above 0.75 were merged.

Gene Ontology analysis. Modules were tested for enrichment of GO terms (categories: molecular function, biological process) using the gProfiler⁶³ R implementation. Module genes were ordered by their kME (module membership) values, and the gene-set enrichment analysis was carried out with the parameters 'ordered_query' set to true, 'max_set_size' limited to 500 and 'hier_filtering' set to strong.

Module and treatment associations. The association between the module eigengene and treatment was tested using logistic regression (Supplementary Data 4). A logistic model with the module eigengene as the dependent variable and treatment group as the independent variable (d.f. = 2) was constructed for each module and compared to the null model (d.f. = 1) using a likelihood-ratio test. *P* values were adjusted for multiple testing using the Bonferroni method (adjusting for the number of modules).

Cell population enrichment for module genes. Cell population marker genes ($ES_{\mu} > 0$) were tested for enrichment of module genes using a one-tailed Fisher's exact test. *P* values were adjusted for multiple testing using the Bonferroni method (adjusting for the number of cell populations × the number of modules).

Pseudo-bulk differential gene expression analysis. A pseudo-bulk gene expression matrix was generated by summing the transcript counts for all cells with the same cell population and sample combination. DESeq2 was applied on the pseudo-bulk gene expression matrix, and *P* values were adjusted for multiple testing using the BH method (adjusting for the number of genes).

Single-nucleus ATAC-sequencing data analysis. **Single-nucleus ATAC-sequencing raw data processing and quality control.** Raw sequencing reads were processed using the Cell Ranger ATAC version 1.1.0 pipeline and aligned to the *Mus musculus* (mm10) genome with default parameters. The aligned reads were further processed using SnapATAC⁶⁴ version 1.0.0. Fragments that were uniquely mapped (mapping quality score > 30) and with proper length (50 bp < length < 1,000 bp) were kept. Based on visual inspection, high-quality cells were detected based on the number of unique fragments and fragments in promoter ratio (selecting cells with $1,000 < \text{unique fragments} < 100,000$; $0.15 < \text{fragments in promoter ratio} < 0.6$). Using these criteria, 29,743 cells were called for downstream analysis.

The genome was segmented into 5-kb bins, and the chromatin accessibility profiles were represented as a binary matrix (1 denoting accessible chromatin; 0

denoting inaccessible chromatin). Bins overlapping blacklisted regions (<http://mitra.stanford.edu/kundaje/akundaje/release/blacklists/>), mapping to unwanted chromosomes (such as mitochondrial, sex or unknown) or exceeding a high coverage (95% quantile), thus likely representing invariant genomic regions, were removed. The binary cell-by-bin matrix was converted to a cell-by-cell distance matrix (Jaccard metric) and was normalized using the regression-based ‘normOVE’ method implemented in SnapATAC. PCA was performed, and PCs 2–40 (determined based on visual inspection of the knee plot and pairwise PCA plots) were subjected to Leiden clustering using the resolution resulting in the highest average silhouette index (resolution: 0.1, 0.2, ..., 1). These steps resulted in 31 clusters (resolution of 0.9). Cells belonging to the same cluster were aggregated, and accessible peaks were called clusterwise using MACS2 (ref. ⁶⁵) version 2.2.6, generating a peak count matrix (253,507 peaks × 29,743 cells). These clusters were solely used to call peaks as described next.

Single-nucleus ATAC-seq cell population identification. A Seurat object was initialized from the peak count matrix. Using Signac⁵⁸ version 0.1.5, the peak count matrix was normalized using term-frequency inverse-document-frequency normalization, and the 95% most common features were identified and used as input for latent semantic indexing dimensionality reduction. The first 30 singular values were used as input for UMAP dimensionality reduction. A gene activity matrix (henceforth ‘pseudo-snRNA-seq matrix’) used for snATAC-seq cell population labelling was computed from the chromatin accessibility within and 2,000 bp upstream of protein-coding genes and stored in the present Seurat object. The gene activity counts for each cell were normalized by its total gene activity, multiplied by the median gene activity across all cells, and log transformed. To annotate cells, canonical correlation analysis and mutual nearest-neighbourhood detection were performed using the Seurat function ‘FindTransferAnchors’ with the snRNA-seq and pseudo-snRNA-seq datasets as inputs. ‘TransferData’ was used to project the labels from the snRNA-seq to the snATAC-seq dataset. Cells with prediction scores below 0.5 were discarded ($n=28$). As the last filtering step, cells with a negative silhouette coefficient computed from the top 30 singular values from the peak count matrix were removed ($n=478$).

The following steps were applied to classify neuronal populations. First, major neuronal populations were identified by projecting labels from the neuronal snRNA-seq dataset to the snATAC-seq dataset as described above. Neurons that could not be confidently classified into one of the 11 neuronal populations (prediction score < 0.5) were discarded ($n=507$). Second, for the snRNA-seq data processing, neurons with a negative silhouette index were removed ($n=3,729$). Third, neuronal population labels were projected from the snRNA-seq dataset, and populations with a prediction score below 0.5 were removed ($n=456$). These filtering steps reduced our snATAC-seq dataset to 11,651 neuronal and 10,894 non-neuronal cells for downstream analysis (total = 22,545). The mean and median number of accessible regions recovered per cell were 7,028 and 4,401, respectively.

Motif analysis. ChromVar⁶⁶ was used to compute z -scores for motif enrichment (one z -score per motif per cell). For each cell population, a logistic regression model was constructed with z -score as the independent variable and cell population as the dependent variable (d.f. = 2) and compared to the null model (d.f. = 1) using a likelihood-ratio test. Enriched motifs (Supplementary Data 5) were identified by averaging ChromVar z -scores for a given motif across cells in a given population, retaining only motifs with an average z -score > 1, and then adjusting P values for multiple testing using the Bonferroni method (adjusting for the number of cell populations × number of motifs).

The following steps were performed to correlate motif enrichment with transcription factor gene expression levels. First, for each cell population, we ranked all transcription factors (up to 334 transcription factors were expressed in our snRNA-seq data) based on their cell population gene expression specificity (mean rank of the four expression specificity metrics used in CELLEX). Second, for each transcription factor and motif pair, the transcription factor rank was correlated (Spearman) with the cell population motif enrichment z -score across all cell populations. A meta P value of the correlation was calculated using Fisher’s method.

Pseudo-bulk differential chromatin accessibility analysis. A pseudo-bulk chromatin accessibility matrix was generated by summing the peak counts for all cells with the same cell population and sample combination. ChromVar was applied on the pseudo-bulk chromatin accessibility matrix to compute z -scores for motif enrichment (one z -score per motif per cell population per sample). To assess differential chromatin accessibility within a cell population, a logistic regression model was constructed with z -score as the independent variable and treatment as the dependent variable (d.f. = 2) and compared to the null model (d.f. = 1) using a likelihood-ratio test. P values were adjusted for multiple testing using the Bonferroni method (adjusting for the number of motifs).

Genetic enrichment analysis. CELLECT analysis. Genetic enrichment analysis was carried out by running CELLECT version 1.0.0 (<https://github.com/perslab/CELLECT/>) on BMI GWAS summary statistics from the UK Biobank comprising >457,000 individuals^{67,68} and the DVC cell population gene expression or

chromatin accessibility profiles. For the gene expression atlas, CELLECT was run on the CELLEX matrix using default parameters (window size of 100 kb). For the chromatin accessibility atlas, the genetic enrichment analysis was carried out using the following steps. Peak coordinates were mapped from the mouse genome build mm10 to the human genome build hg19 using liftOver with the ‘minMatch’ parameter set to 0.1 (recommended parameter value for cross-species mapping). Eighty-three percent of the peaks could be mapped to the human genome. For each cell population, all peaks containing ≥ 1 enriched motif ($z > 1$) and Bonferroni-adjusted $P < 0.05$) were ranked based on their maximum z -score and rank normalized to values between 0 and 1. Remaining peaks were assigned a value of 0. The resulting cell population-by-peak matrix was used as input for CELLECT using a window size of 1 kb as used in work by Rai et al.⁶⁹. For both genetic enrichment analyses, P values were corrected for multiple testing using the Bonferroni method (adjusting for the number of cell populations).

Meta-analysis. One-tailed meta-analysis (Supplementary Data 6) was performed with the ‘metafor’ R package with the ‘rma.uni’ function using the fixed-effects method with CELLECT coefficients as input values and CELLECT precision as weights. The meta-analysis P values were corrected for multiple testing using the Bonferroni method (adjusting for the number of cell populations).

Immunohistochemistry and RNA in situ hybridization. All procedures were conducted in accordance with national regulations in Denmark, which are fully compliant with internationally accepted principles for the care and use of laboratory animals, and with animal experimental licences granted by the Danish Ministry of Justice. Six C57BL/6 male mice aged 8 weeks were dosed with Ex4 (i.v., 200 µg kg⁻¹; $n=2$) or vehicle ($n=4$) for 2 h, then killed and perfusion fixed with formalin, and the brains were removed and embedded in paraffin after post-fixing in formalin overnight. Immersion-fixed brain samples collected at necropsy from two cynomolgous monkeys (1 male, 7 years old; 1 female, 5 years old) were purchased from Charles River and were embedded in paraffin after receipt. Samples were cut (4 µm), and sections with AP areas represented (2–5 sections for each animal) were used for automated RNAscope (ACD, Bio-Techne) duplex ISH/ISH with chromogenic substrates or ISH/IHC fluorescence protocols on the Ventana Discovery Ultra platform using RNAscope VS automated workflows⁷⁰, using the following probes and antibodies: mouse probes (ACDBio, Bio-Techne): Ramp3 (497139), Glp1r (418859), Casr (423459), Gfral (439149), Olfr78 (436609), Grpr (317879), Asb4 (435099), Gipr (455789), Ccbe1 (485659), Bdnf-C2 (316039-C2), Mc4r-C2 (319189-C2), Glp1r-C2 (418859-C2), Lepr-C2 (471179-C2), Gcg-C2 (400609-C2), Gipr-C2 (319129-C2), Pax5-C2 (319189-C2) and Calcr-C2 (494079-C2); primate probes (ACDBio, Bio-Techne): Mfa-Ramp3-C2 (486679-C2), Mmu-Glp1r-C2 (449299-C2), Mfa-Casr (481659), Hs-Gfral (483049) and Hs-Calcr (483049); negative-control probes (ACDBio, Bio-Techne): Dabp (312039) and Dabp-C2 (312039-C2); rodent GLP-1R (monoclonal rabbit) antibody: ab218532, Abcam (1:200). Fluorescence slides were scanned on an Olympus VS120 scanner, and slides developed using chromogens were scanned on a Hamamatsu Nanozoomer XR scanner.

Cre-transgenic mouse studies. Mice. Mice were bred in the colony in the Unit for Laboratory Animal Medicine at the University of Michigan; these mice and procedures were approved by the University of Michigan Committee on the Use and Care of Animals and in accordance with Association for the Assessment and Approval of Laboratory Animal Care and National Institutes of Health (NIH) guidelines. C57BL/6 male mice aged 8 to 12 weeks were purchased from the Jackson Laboratory. Mice were provided with standard chow diet (Purina Lab Diet 5001; except as noted below) and water ad libitum in temperature-controlled rooms on a 12-h light/dark cycle. *Calcr-Cre* mice⁷¹ were propagated by intercrossing homozygous mice of the same genotype and used for the DREADD experiments. The *Glp1r-Cre* or *Calcr-Cre* line crossed with Cre-inducible GFP reporter mice were used for IHC.

Viral reagents and stereotaxic injections. AAV8-hSyn-DIO-hM3Dq-mCherry⁷² was prepared by the University of North Carolina Vector Core. For NTS injection, following the induction of isoflurane anaesthesia and placement in a stereotaxic frame, the skulls of adult mice were exposed. The obex was set as the reference point for injection. After the reference was determined, a guide cannula with a pipette injector was lowered into the approximate NTS coordinates (A/P, -0.2; M/L, ±0.2; D/V, -0.2) from the obex, and 100 nl of virus was injected using a picospritzer at a rate of 5–30 nl min⁻¹ with pulses. Five minutes following injection, to allow for adequate dispersal and absorption of the virus, the injector was removed from the animal, and the incision site was closed and glued. The mice received prophylactic analgesics before and after surgery.

Phenotypic assessment. DREADD-expressing mice and their controls were treated with CNO (4936, Tocris; i.p., 1 mg kg⁻¹) at the onset of dark cycle. For long-term standard chow or 60% HFD (Research Diets, D12492) food intake and body weight assessment, DREADD-expressing mice (chow, $n=7$; HFD, $n=7$) and their controls (chow, $n=6$; HFD, $n=5$) were given saline for 2–3 d before injection of CNO twice per day (approximately 17:30 and 08:30) for 2 d, followed

by saline injections for another 1–2 d to assess recovery from the treatment. For short-term HFD food intake assessment, food intake was monitored over 4 h in the dark cycle in DREADD-expressing mice after administration of saline ($n=7$) or CNO ($n=7$). To assess the effect of CNO on short-term food intake, chow food intake was monitored over 4 h in the dark cycle in wild-type mice injected with hM3Dq-mCherry in the NTS after administration with saline ($n=6$) or CNO (i.p., 1 mg kg $^{-1}$; $n=6$). To assess the effect of CNO on long-term food intake, chow food intake was monitored over 24 h in wild-type mice injected with hM3Dq-mCherry in the NTS after administration with saline ($n=6$) or CNO (i.v., 1 mg kg $^{-1}$; $n=6$).

Immunohistochemistry. Mice were anaesthetized with isoflurane and perfused with PBS followed by 10% buffered formalin. Brains were removed, placed in 10% buffered formalin overnight and dehydrated in 30% sucrose for 1 week. With use of a freezing microtome (Leica), brains were cut into 30-μm sections. Sections were treated sequentially with 1% hydrogen peroxide/0.5% sodium hydroxide, 0.3% glycine, 0.03% sodium dodecyl sulfate and blocking solution (PBS with 0.1% Triton X-100 and 3% normal donkey serum). Three mice were used for the assessment of TH and DDC expression. For Ex4 FOS studies, mice were treated with saline (i.p., $n=3$) or Ex4 (6355, Tocris; i.p., 150 μg kg $^{-1}$; $n=3$) 2 h before perfusion. For sCT FOS studies, mice were treated with sCT (4033011, Bachem; i.p., 150 μg kg $^{-1}$; $n=3$) 2 h before perfusion. The perfused sections were incubated overnight at room temperature in rabbit anti-FOS (FOS, 2250, Cell Signaling Technology; 1:1,000) and exposed the next day with fluorescent secondary antibody (Molecular Probes, 1:200) to visualize proteins. Immunofluorescence staining was performed using primary antibodies (GFP, GFP1020, Aves Laboratories, 1:1,000 dilution; dsRed, 632496, Takara, 1:1,000 dilution; TH, NB300-109, Novus Biologicals, 1:1,000 dilution; DDC, 101661-AP, Proteintech, 1:1,000 dilution). Antibodies were reacted with species-specific Alexa Fluor 488-, 568- or 647-conjugated secondary antibodies (Invitrogen, Thermo Fisher; 1:200 dilution). Images were collected on an Olympus BX53F microscope. Images were pseudo-coloured using Photoshop (Adobe) or Image J (NIH).

In vivo study data statistical analyses. Statistical analyses on mouse in vivo study data were performed by constructing a linear mixed-effects model with food intake or body weight as the dependent variable, genotype and time point as independent variables with interaction effects, and mouse as the random effect. Group contrasts were tested using a least-squares means two-tailed *t*-test, and *P* values were adjusted for multiple testing using the Bonferroni method.

Cre-transgenic rat studies. Rats. Rats were bred in the Unit for Laboratory Animal Medicine at the University of Michigan; these rats and the procedures performed were approved by the University of Michigan Committee on the Use and Care of Animals and in accordance with Association for the Assessment and Approval of Laboratory Animal Care and NIH guidelines. Wild-type Sprague-Dawley rats were obtained from Charles River Laboratories.

Calcr-Cre rats were produced by CRISPR-Cas9-mediated gene editing in collaboration with the Molecular Genetics Core of the Michigan Diabetes Research Center. Briefly, we designed standard guide RNAs homologous to opposite-stranded sequences beginning 24 and 73 bp downstream of the end of the coding sequences (guide RNA sequences: CTCAGTGGATCACATGTTG and TGGGATCACTGAAACCGCA). Synthetic single-guide RNAs containing these sequences (Synthego) were co-injected into fertilized oocytes together with Cas9 protein and an editing template containing the 200-bp 5'- and 3'-homology arms surrounding sequences for a self-cleaving P2A peptide plus coding sequences for a nuclear-localized Cre recombinase in place of the CALCR STOP codon plus the subsequent 93 bp of genomic sequences (Supplementary Fig. 3a). The embryos were implanted into pseudopregnant females, and all pups were genotyped for the presence of *Cre*. *Cre*-containing pups were subjected to long-range PCR to determine insertion of the desired sequences in the correct genomic locus (Supplementary Fig. 3b); these genomic fragments were also subjected to Sanger sequencing to ensure the lack of adventitious mutations. Eight out of 78 were positive founders.

By applying IHC, we later confirmed that AP *Cre* reporter activity was specific to *Calcr* cells (Supplementary Fig. 3c). *Calcr-Cre* rats were bred to *ROSA26*^{em1(CAG-tdTomato)} reporter rats (purchased from Sigma Advanced Genetic Engineering Labs), and offspring were genotyped and confirmed by DNA sequencing, as above. Rats were housed in a 12-h light/dark cycle at a 21°C constant temperature. All rats were housed in cages with Bed-O'Cobs bedding with ad libitum access to standard chow and Lixit water, except during the experiment.

Genotyping and PCR analysis. *Calcr-Cre* rats were genotyped using the following primers for *Calcr-Cre*: 5' Cre-TATCAACTCGCGCCCTGGAAG 3' and 5' *Calcr* 3' HA-TATTTGGGTCTGCCTGGTGAC 3'; expected size of 748 bp. *ROSA26*^{em1(CAG-tdTomato)} reporter rats were genotyped for tdTomato using the following primers: CAG-3F-GCAACGTGCTGGTTATTGTG and tdTomato-5R-TGATGACCTCCTGCCCTTG; expected band size of 550 bp.

Viral reagents and stereotaxic injections. Before surgery, 6- to 12-month-old *Calcr-Cre* female rats ($n=6$; 250–400 g) were handled for 3 min for 3 d. Rats were

anaesthetized with isoflurane (induced in a chamber at 3% and maintained under anaesthesia at 2–2.5%, delivered via face mask). Oxygen flow was delivered at 0.81 min $^{-1}$. Rats received buprenorphine hydrochloride (s.c., 0.03 mg kg $^{-1}$), Buprenex and carprofen (s.c., 5 mg kg $^{-1}$) injections before brain stereotaxic surgery (Model 942 Kopf with digital display console). Rats were placed on the stereotaxic frame with their head inclined to about a 90° angle. To reach the AP, an incision was made on the skin and three muscles on a rostrocaudal axis direction. An incision was made from left to right (horizontally) to reveal the fourth ventricle; the AP and the obex are found caudal of the fourth ventricle. Rats received an AAV8-hSyn-DIO-hM3Dq-mCherry⁷² virus injection in the AP ($Z=-0.3$ mm) of a volume of 500 nl using a Hamilton syringe (5-μl syringe 800 series, 33-gauge small hub RN needle). Rats continued to receive Buprenex (twice a day; 3 d in total) and carprofen (once a day; 3 d in total). They received post-operative care for 7–10 d after their sutures were removed. Twenty-one days were allowed before experimentation for the virus to be expressed.

Phenotypic assessment. Rats were moved to an experimental room and placed in a new cage set-up (Pure-O'CeI bedding and water bottles). They received 3 d of handling and habituation in their new room and cage. They received CNO (4936, Tocris; i.p., 1 mg kg $^{-1}$) or 0.9% sodium chloride injection (i.p., 1 mg kg $^{-1}$) 30 min before the onset of the dark cycle. Additionally, food measures were collected at the following time points (onset of dark cycle): 2, 4, 6, 16 and 24 h. After a week, conditions were counterbalanced among rats. Animals that received CNO on the first trial received saline on the second trial and vice versa. Following these experiments, rats were perfused under anaesthesia and processed for the detection of mCherry (as below). Animals lacking AP mCherry-IR or with mCherry-IR outside of the AP were excluded from further analysis (two animals were excluded, leaving four animals in the final analysis). To assess the effect of CNO on food intake, 3- to 4-month-old *Calcr-Cre* female rats ($n=10$) received CNO (4936, Tocris; i.p., 1 mg kg $^{-1}$) or 0.9% sodium chloride injection (i.p., 1 mg kg $^{-1}$) 30 min before the onset of the dark cycle, and food measures were collected as above. Likewise, after a week, conditions were counterbalanced among rats, and animals that received CNO on the first trial received saline on the second trial and vice versa.

Immunohistochemistry. Rats were placed under CO₂ and then transcardially perfused with PBS and 10% buffered formalin. Brains were extracted and placed in 10% buffered formalin overnight and cryoprotected in 30% sucrose. The brains were coronally sectioned into 30-μm sections using a microtome (Leica). Sections were washed in PBS and placed in PBS with 0.1% Triton X-100 and 3% normal donkey serum blocking solution. Tissue was incubated overnight at room temperature in dsRed at 1:1,000 dilution (Rabbit, 632392, Takara Bio Clontech). The tissue was incubated in Alexa Fluor 568 secondary antibody.

Rat in vivo study statistical analyses. Statistical analyses were carried out as described above for the mouse in vivo studies, using food intake as the dependent variable, treatment (CNO or saline) and time point as independent variables with interaction effects, and sample as the random effect. Group contrasts were tested using least-squares means, and *P* values were adjusted for multiple testing using the Bonferroni method.

Reporting Summary. Further information on research design is available in the Nature Research Reporting Summary linked to this article.

Data availability

All genetic data generated in this study (bulk RNA-seq, snRNA-seq and snATAC-seq) are available in the GEO under SuperSeries accession number [GSE166649](#). All other data are available from the authors upon reasonable request. Source data are provided with this paper.

Code availability

The source code used to analyse the data and produce the statistical figures is available at <https://github.com/perslab/Ludwig-2021/>.

Received: 8 July 2020; Accepted: 16 February 2021;

Published online: 25 March 2021

References

- Bray, G. A. Medical treatment of obesity: the past, the present and the future. *Best Pract. Res. Clin. Gastroenterol.* **28**, 665–684 (2014).
- Bray, G. A., Frühbeck, G., Ryan, D. H. & Wilding, J. P. H. Management of obesity. *Lancet* **387**, 1947–1956 (2016).
- Schwartz, M. W. et al. Obesity pathogenesis: an endocrine society scientific statement. *Endocr. Rev.* **38**, 267–296 (2017).
- O'Rahilly, S. & Farooqi, I. S. Genetics of obesity. *Philos. Trans. R. Soc. Lond. B Biol. Sci.* **361**, 1095–1105 (2006).
- Srivastava, G. & Caroline, M. Current pharmacotherapy for obesity. *Nat. Rev. Endocrinol.* **14**, 12–24 (2018).

6. Locke, A. E. et al. Genetic studies of body mass index yield new insights for obesity biology. *Nature* **518**, 197–206 (2015).
7. Timshel, P. N., Thompson, J. J. & Pers, T. H. Genetic mapping of etiologic brain cell types for obesity. *eLife* **9**, e55851 (2020).
8. Grill, H. J. & Hayes, M. R. Hindbrain neurons as an essential hub in the neuroanatomically distributed control of energy balance. *Cell Metab.* **16**, 296–309 (2012).
9. Jensen, C. B. et al. Characterization of the glucagonlike peptide-1 receptor in male mouse brain using a novel antibody and *in situ* hybridization. *Endocrinology* **159**, 665–675 (2018).
10. Cork, S. C. et al. Distribution and characterisation of glucagon-like peptide 1 receptor expressing cells in the mouse brain. *Mol. Metab.* **4**, 718–731 (2015).
11. Mulligan, S. E. et al. GFRAL is the receptor for GDF15 and the ligand promotes weight loss in mice and non-human primates. *Nat. Med.* **23**, 1150–1157 (2017).
12. Christopoulos, G. et al. Multiple amylin receptors arise from receptor activity-modifying protein interaction with the calcitonin receptor gene product. *Mol. Pharmacol.* **56**, 235–242 (1999).
13. Adriaenssens, A. E. et al. Glucose-dependent insulinotropic polypeptide receptor-expressing cells in the hypothalamus regulate food intake. *Cell Metab.* **30**, 987–996 (2019).
14. Braegger, F. E., Asarian, L., Dahl, K., Lutz, T. A. & Boyle, C. N. The role of the area postrema in the anorectic effects of amylin and salmon calcitonin: behavioral and neuronal phenotyping. *Eur. J. Neurosci.* **40**, 3055–3066 (2014).
15. Richard, J. E. et al. Activation of the GLP-1 receptors in the nucleus of the solitary tract reduces food reward behavior and targets the mesolimbic system. *PLoS ONE* **10**, e0119034 (2015).
16. Hayes, M. R. et al. Intracellular signals mediating the food intake suppressive effects of hindbrain glucagon-like-peptide-1 receptor activation. *Cell Metab.* **13**, 320–330 (2011).
17. Cheng, W. et al. Calcitonin receptor neurons in the mouse nucleus tractus solitarius control energy balance via the non-aversive suppression of feeding. *Cell Metab.* **31**, 301–312 (2020).
18. Coester, B., Foll, C. L. & Lutz, T. A. Viral depletion of calcitonin receptors in the area postrema: a proof-of-concept study. *Physiol. Behav.* **223**, 112992 (2020).
19. Stuart, T. & Satija, R. Integrative single-cell analysis. *Nat. Rev. Genet.* **20**, 257–272 (2019).
20. Bentsen, M. A. et al. Transcriptomic analysis links diverse hypothalamic cell types to fibroblast growth factor 1-induced sustained diabetes remission. *Nat. Commun.* **11**, 1–16 (2020).
21. Inoue, F. et al. Genomic and epigenomic mapping of leptin-responsive neuronal populations involved in body weight regulation. *Nat. Metab.* **1**, 475–484 (2019).
22. Campbell, J. N. et al. A molecular census of arcuate hypothalamus and median eminence cell types. *Nat. Neurosci.* **20**, 484–496 (2017).
23. O’Neil, P. M. et al. Efficacy and safety of semaglutide compared with liraglutide and placebo for weight loss in patients with obesity: a randomised, double-blind, placebo and active controlled, dose-ranging, phase 2 trial. *Lancet* **392**, 637–649 (2018).
24. Adams, J. M. et al. Liraglutide modulates appetite and body weight through glucagon-like peptide 1 receptor-expressing glutamatergic neurons. *Diabetes* **67**, 1538–1548 (2018).
25. Gabery, S. et al. Semaglutide lowers body weight in rodents via distributed neural pathways. *JCI Insight* **5**, e133429 (2020).
26. Langlet, F., Mullier, A., Bouret, S. G., Prevot, V. & Dehouck, B. Tanycyte-like cells form a blood–cerebrospinal fluid barrier in the circumventricular organs of the mouse brain. *J. Comp. Neurol.* **521**, 3389–3405 (2013).
27. Lein, E. S. et al. Genome-wide atlas of gene expression in the adult mouse brain. *Nature* **445**, 168–176 (2007).
28. Katsurada, K. et al. Central glucagon-like peptide 1 receptor signaling via brainstem catecholamine neurons counteracts hypertension in spontaneously hypertensive rats. *Sci. Rep.* **9**, 1–13 (2019).
29. Holt, M. K. et al. Preproglucagon neurons in the nucleus of the solitary tract are the main source of brain GLP-1, mediate stress-induced hypophagia, and limit unusually large intakes of food. *Diabetes* **68**, 21–33 (2019).
30. Cheng, W. et al. Leptin receptor-expressing nucleus tractus solitarius neurons suppress food intake independently of GLP1 in mice. *JCI Insight* **5**, e134359 (2020).
31. Allison, M. B. et al. Defining the transcriptional targets of leptin reveals a role for Atf3 in leptin action. *Diabetes* **67**, 1093–1104 (2018).
32. Yang, C. et al. Paired-like homeodomain proteins, Phox2a and Phox2b, are responsible for noradrenergic cell-specific transcription of the dopamine beta-hydroxylase gene. *J. Neurochem.* **71**, 1813–1826 (1998).
33. Bahrami, S. & Drablos, F. Gene regulation in the immediate-early response process. *Adv. Biol. Regul.* **62**, 37–49 (2016).
34. Frikke-Schmidt, H. et al. GDF15 acts synergistically with liraglutide but is not necessary for the weight loss induced by bariatric surgery in mice. *Mol. Metab.* **21**, 13–21 (2019).
35. Barth, S. B., Riediger, T., Lutz, T. A. & Reckemmer, G. Peripheral amylin activates circumventricular organs expressing calcitonin receptor a/b subtypes and receptor-activity modifying proteins in the rat. *Brain Res.* **997**, 97–102 (2004).
36. Gross, P. M. Circumventricular organ capillaries. *Prog. Brain Res.* **91**, 219–233 (1992).
37. Zhang, C. et al. Area postrema cell types that mediate nausea-associated behaviors. *Neuron* **109**, 1–12 (2021).
38. Gaykema, R. P. et al. Activation of murine pre-proglucagon-producing neurons reduces food intake and body weight. *J. Clin. Invest.* **127**, 1031–1045 (2017).
39. Berglund, E. D. et al. Melanocortin 4 receptors in autonomic neurons regulate thermogenesis and glycemia. *Nat. Neurosci.* **17**, 911–913 (2014).
40. Resch, J. M. et al. Aldosterone-sensing neurons in the NTS exhibit state-dependent pacemaker activity and drive sodium appetite via synergy with angiotensin II signaling. *Neuron* **96**, 190–206 (2017).
41. Do, J., Chang, Z., Sekerková, G., McGrimon, D. R. & Martina, M. A leptin-mediated neural mechanism linking breathing to metabolism. *Cell Rep.* **33**, 108358 (2020).
42. Brierley, D. I. et al. Central and peripheral GLP-1 systems independently suppress eating. *Nat. Metab.* **3**, 258–273 (2021).
43. Ranadive, S. A. & Vaisse, C. Lessons from extreme human obesity: monogenic disorders. *Endocrinol. Metab. Clin. North Am.* **37**, 733–751 (2008).
44. Philippe, J. et al. A nonsense loss-of-function mutation in PCSK1 contributes to dominantly inherited human obesity. *Int. J. Obes.* **39**, 295–302 (2015).
45. Baroohay, B., Lebrun, B., Moyse, E. & Jean, A. Brain-derived neurotrophic factor plays a role as an anorexigenic factor in the dorsal vagal complex. *Endocrinology* **146**, 5612–5620 (2005).
46. Williams, D. L., Kaplan, J. M. & Grill, H. J. The role of the dorsal vagal complex and the vagus nerve in feeding effects of melanocortin-3/4 receptor stimulation. *Endocrinology* **141**, 1332–1337 (2000).
47. Fortin, S. M., Chen, J. & Hayes, M. R. Hindbrain melanocortin 3/4 receptors modulate the food intake and body weight suppressive effects of the GLP-1 receptor agonist, liraglutide. *Physiol. Behav.* **220**, 112870 (2020).
48. Alhadeff, A. L. et al. Endogenous glucagon-like peptide 1 receptor signaling in the nucleus tractus solitarius is required for food intake control. *Neuropsychopharmacology* **42**, 1471–1479 (2017).
49. Hayes, M. R., Bradley, L. & Grill, H. J. Endogenous hindbrain glucagon-like peptide 1 receptor activation contributes to the control of food intake by mediating gastric satiation signaling. *Endocrinology* **150**, 2654–2659 (2009).
50. Borner, T. et al. GDF15 induces anorexia through nausea and emesis. *Cell Metab.* **31**, 351–362 (2020).
51. Ahrén, B. et al. Semaglutide induces weight loss in subjects with type 2 diabetes regardless of baseline BMI or gastrointestinal adverse events in the SUSTAIN 1 to 5 trials. *Diabetes Obes. Metab.* **20**, 2210–2219 (2018).
52. Georgescu, T. et al. Neurochemical characterization of brainstem pro-opiomelanocortin cells. *Endocrinology* **161**, 1–13 (2020).
53. Secher, A. et al. The arcuate nucleus mediates GLP-1 receptor agonist liraglutide-dependent weight loss. *J. Clin. Invest.* **124**, 4473–4488 (2014).
54. Baraboi, E. D., Smith, P., Ferguson, A. V. & Richard, D. Lesions of area postrema and subfornical organ Alter exendin-4-induced brain activation without preventing the hypophagic effect of the GLP-1 receptor agonist. *Am. J. Physiol. Regul. Integr. Comp. Physiol.* **298**, R1098–R1110 (2010).
55. Love, M. I., Huber, W. & Anders, S. Moderated estimation of fold change and dispersion for RNA-seq data with DESeq2. *Genome Biol.* **15**, 550 (2014).
56. Wang, R., Nambiar, R., Zheng, D. & Tian, B. PolyA_DB 3 catalogs cleavage and polyadenylation sites identified by deep sequencing in multiple genomes. *Nucleic Acids Res.* **46**, D315–D319 (2018).
57. Haeussler, M. et al. The UCSC genome browser database: 2019 update. *Nucleic Acids Res.* **47**, D853–D858 (2019).
58. Stuart, T. et al. Comprehensive integration of single-cell data. *Cell* **177**, 1888–1902 (2019).
59. McGinnis, C. S., Murrow, L. M. & Gartner, Z. J. DoubletFinder: doublet detection in single-cell RNA-sequencing data using artificial nearest neighbors. *Cell Syst.* **8**, 329–337 (2019).
60. Langfelder, P. & Horvath, S. WGCNA: an R package for weighted correlation network analysis. *BMC Bioinformatics* **9**, 559 (2008).
61. Chen, R., Wu, X., Jiang, L. & Zhang, Y. Single-cell RNA-seq reveals hypothalamic cell diversity. *Cell Rep.* **18**, 3227–3241 (2017).
62. Romanov, R. A. et al. Molecular interrogation of hypothalamic organization reveals distinct dopamine neuronal subtypes. *Nat. Neurosci.* **20**, 176–188 (2017).
63. Raudvere, U. et al. gProfil: a web server for functional enrichment analysis and conversions of gene lists. *Nucleic Acids Res.* **47**, W191–W198 (2019).
64. Fang, R. et al. Comprehensive analysis of single cell ATAC-seq data with SnapATAC. *Nat. Commun.* **12**, 1337 (2021).
65. Zhang, Y. et al. Model-based analysis of ChIP-Seq (MACS). *Genome Biol.* **9**, 1–9 (2008).
66. Schep, A. N., Wu, B., Buenrostro, J. D. & Greenleaf, W. J. chromVAR: inferring transcription-factor-associated accessibility from single-cell epigenomic data. *Nat. Methods* **14**, 975–978 (2017).

67. Bycroft, C. et al. The UK Biobank resource with deep phenotyping and genomic data. *Nature* **562**, 203–209 (2018).
68. Loh, P. R., Kichaev, G., Gazal, S., Schoech, A. P. & Price, A. L. Mixed-model association for biobank-scale datasets. *Nat. Genet.* **50**, 906–908 (2018).
69. Rai, V. et al. Single-cell ATAC-seq in human pancreatic islets and deep learning upscaling of rare cells reveals cell-specific type 2 diabetes regulatory signatures. *Mol. Metab.* **32**, 109–121 (2020).
70. Pyke, C. Automated ISH for validated histological mapping of lowly expressed genes. *Methods Mol. Biol.* **2148**, 219–228 (2020).
71. Pan, W. et al. Essential role for hypothalamic calcitonin receptor-expressing neurons in the control of food intake by leptin. *Endocrinology* **159**, 1860–1872 (2018).
72. Krashes, M. J. et al. Rapid, reversible activation of AgRP neurons drives feeding behavior in mice. *J. Clin. Invest.* **121**, 1424–1428 (2011).

Acknowledgements

Novo Nordisk Foundation Center for Basic Metabolic Research is an independent research centre, based at the University of Copenhagen, and partially funded by an unconditional donation from the Novo Nordisk Foundation (<https://www.cbmr.ku.dk/>; grant no. NNF18CC0034900). We acknowledge the Novo Nordisk Foundation (grant no. NNF16OC0021496 to T.H.P.) and the Lundbeck Foundation (grant no. R190-2014-3904 to T.H.P.). We acknowledge J. J. Thompson from the Single-Cell Omics Platform at the Novo Nordisk Foundation Center for Basic Metabolic Research for help with uploading the data to the GEO database. Furthermore, this work was supported by a research grant from the Danish Diabetes Academy, which is funded by the Novo Nordisk Foundation (grant no. NNF17SA0031406). Studies at the University of Michigan were funded by the NIH (P01DK117821 to M.G.M.), BioPharmaceuticals R&D, AstraZeneca (to M.G.M.), the American Diabetes Association (1-16-PDF-021 to W.C.) and supported by the Michigan Diabetes Research Center Molecular Genetics Core (P30DK020572).

Author contributions

M.Q.L., W.C., D.G., J.L., S.J.P., S.N.H., K.L.E., P.B., C.J.R., A.S., L.B.K., C.P., M.G.M. and T.H.P. designed the experiments. W.C., S.J.P., S.N.H. and P.B. performed the mouse experiments. D.G. performed the rat experiments. J.L., S.J.P. and K.L.E. performed the single-nucleus experiments. M.Q.L. analysed the data. M.Q.L., M.G.M. and T.H.P. wrote the initial draft of the manuscript, and all authors edited, read and approved the final version. T.H.P. is the guarantor of the manuscript.

Competing interests

P.B. is employed by Gubra. S.J.P., S.N.H., A.S., L.B.K. and C.P. are employed by Novo Nordisk A/S. C.J.R. is employed by AstraZeneca and holds stock in the company. All other authors declare no competing interests.

Additional information

Extended data is available for this paper at <https://doi.org/10.1038/s42255-021-00363-1>.

Supplementary information The online version contains supplementary material available at <https://doi.org/10.1038/s42255-021-00363-1>.

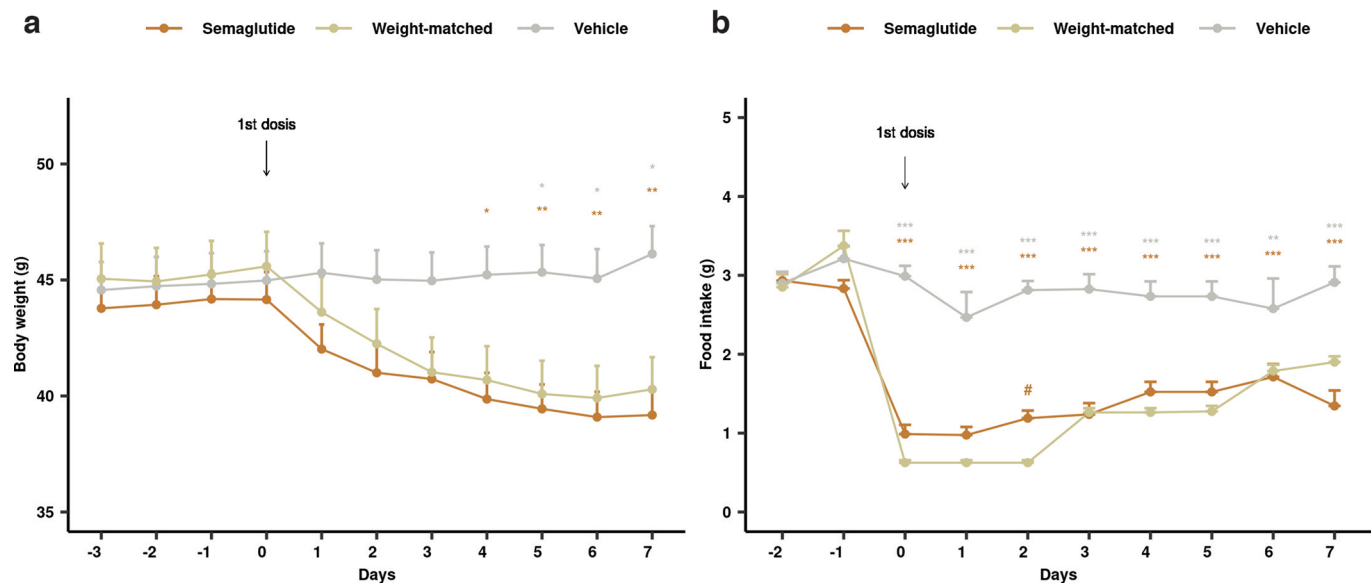
Correspondence and requests for materials should be addressed to T.H.P.

Peer review information *Nature Metabolism* thanks Zachary Knight, Karolina P. Skibicka and the other, anonymous, reviewer(s) for their contribution to the peer review of this work. Primary Handling Editor: Christoph Schmitt.

Reprints and permissions information is available at www.nature.com/reprints.

Publisher's note Springer Nature remains neutral with regard to jurisdictional claims in published maps and institutional affiliations.

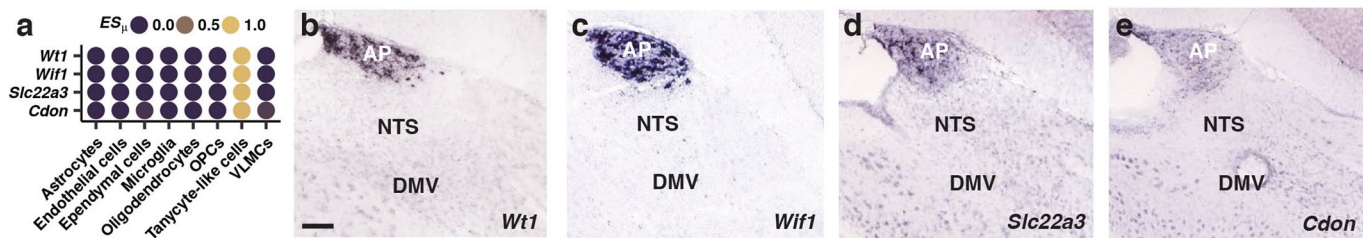
© The Author(s), under exclusive licence to Springer Nature Limited 2021



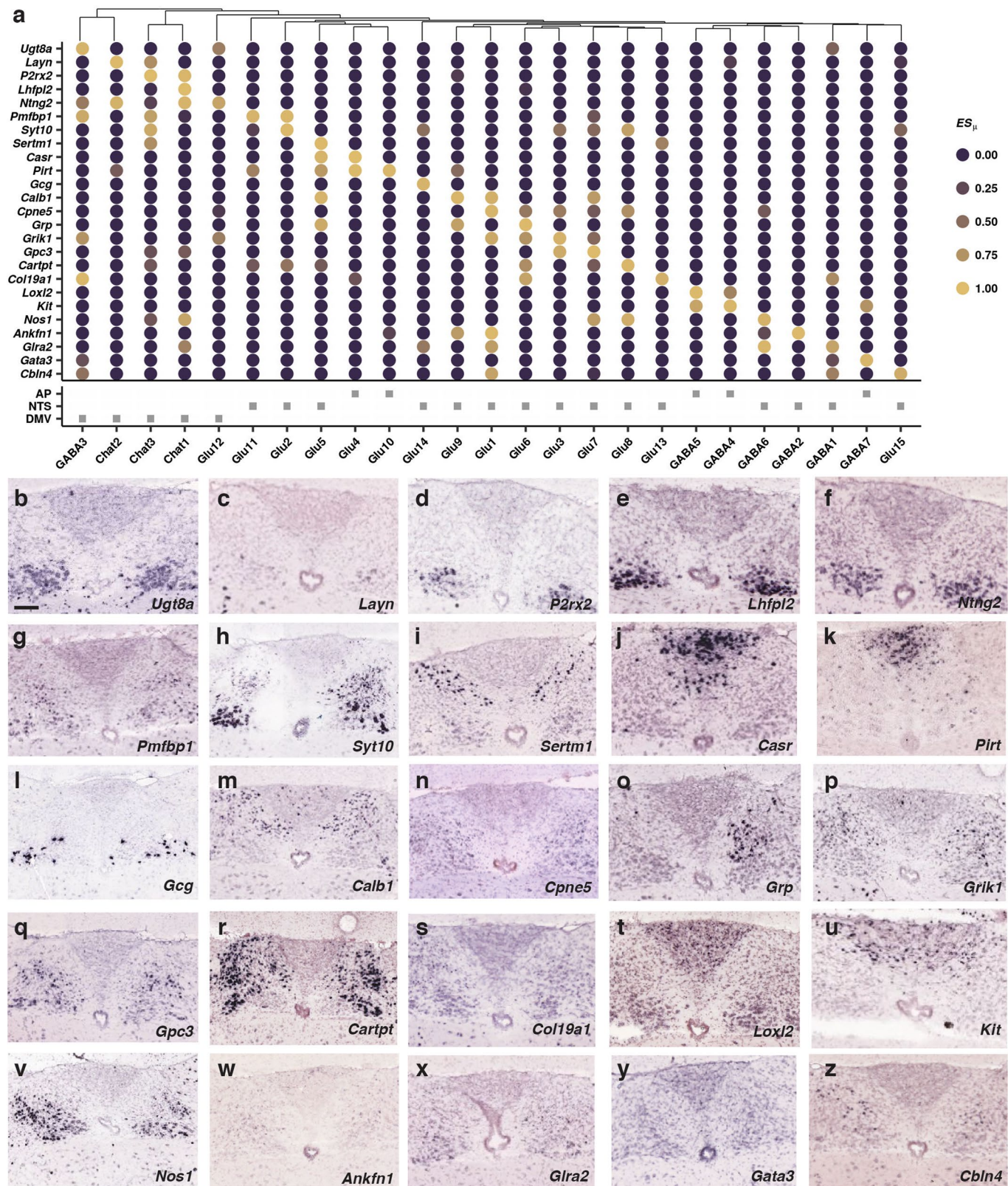
Extended Data Fig. 1 | Body weight and food intake for the single-nucleus RNA- and ATAC-seq *in vivo* study. **a,b,** Daily body weight (**a**) and food intake

(**b**) in semaglutide-administered (n=9), ad libitum-fed vehicle-administered (n=9) and weight-matched control mice (n=8). Values are mean \pm s.e.m.

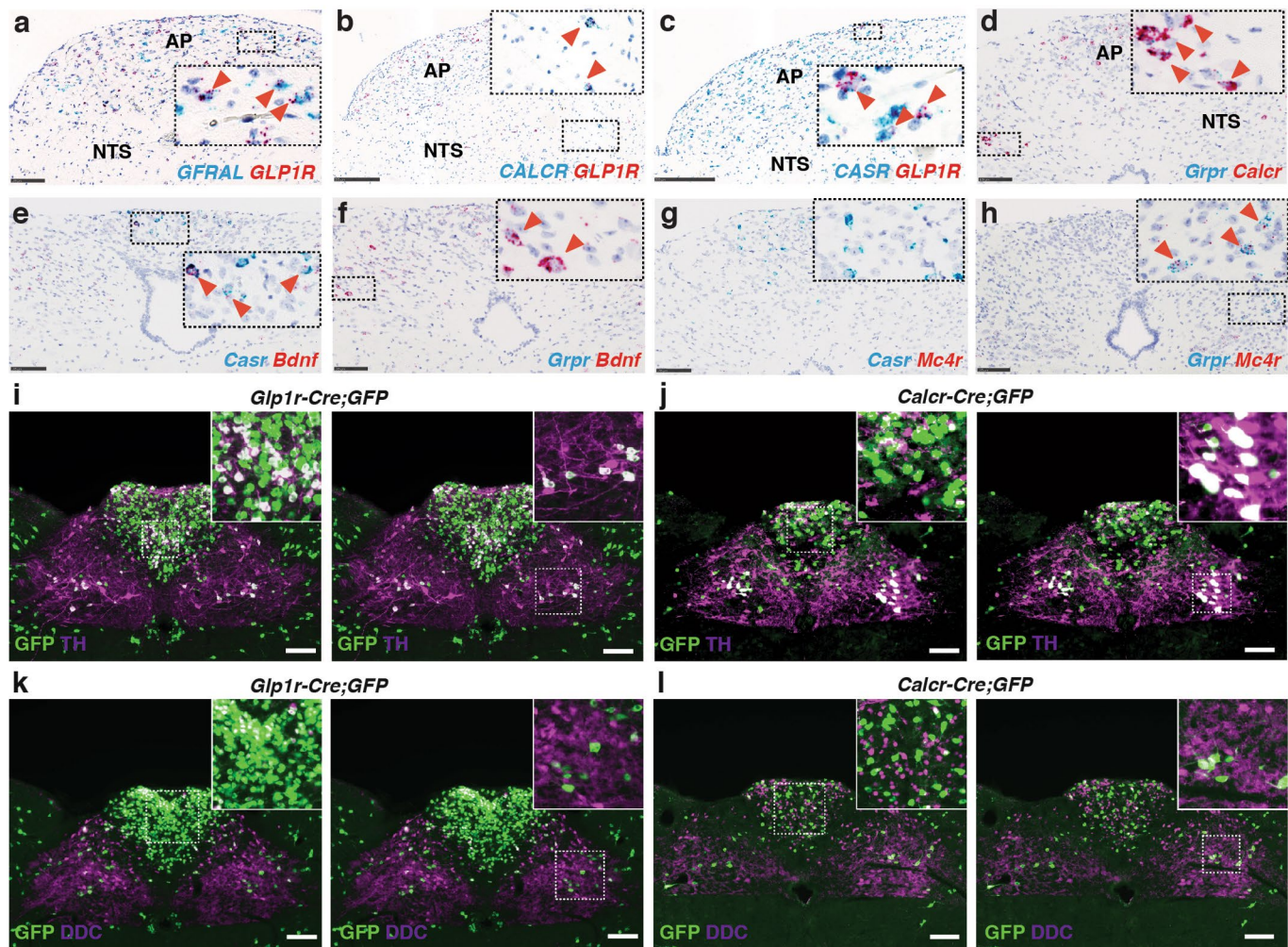
*P<0.05, **P<0.01, ***P<0.001 versus vehicle and #P<0.05, ##P<0.01, ###P<0.001 semaglutide versus weight-matched, linear mixed effects model, Bonferroni-adjusted least-squares means two-tailed t-test.



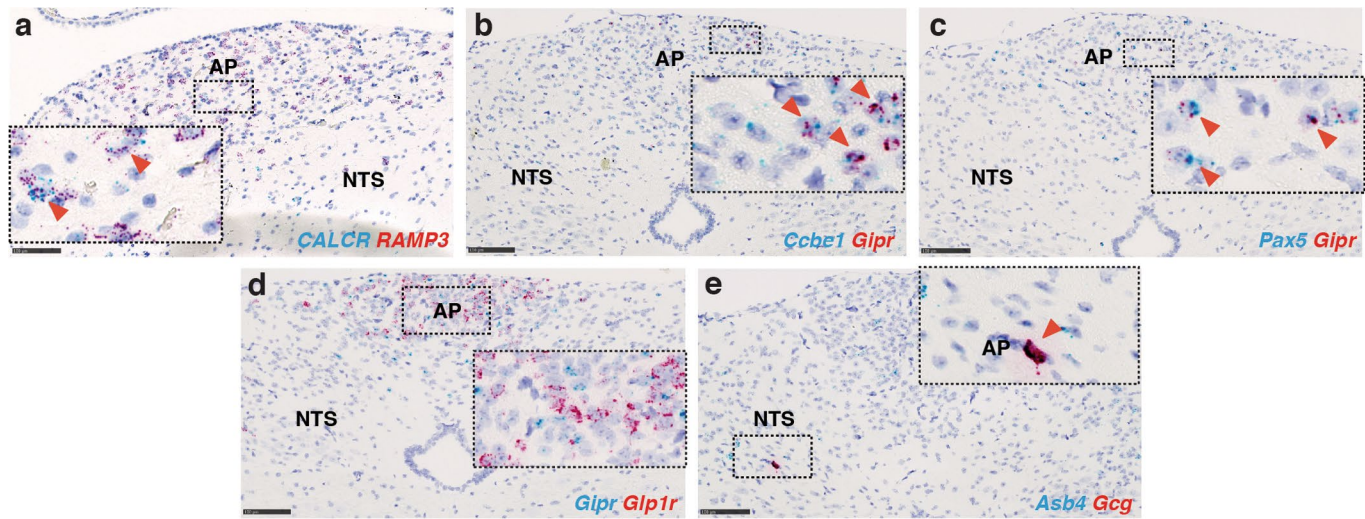
Extended Data Fig. 2 | Expression of tanyocyte-like cell marker genes. **a**, Expression of marker genes for tanyocyte-like cells. **b-e**, ISH of sagittal brain sections (Allen Mouse Brain Atlas) of *Wt1* (n=1 mouse) (**b**), *Wif1* (n=2 mice) (**c**), *Slc22a3* (n=1 mouse) (**d**) and *Cdon* (n=1 mouse) (**e**). Scale bar for panel **b** is representative for panels **c-e**, 100 μ m. Data for reconstruction of **a** are available in Supplementary Data 2.



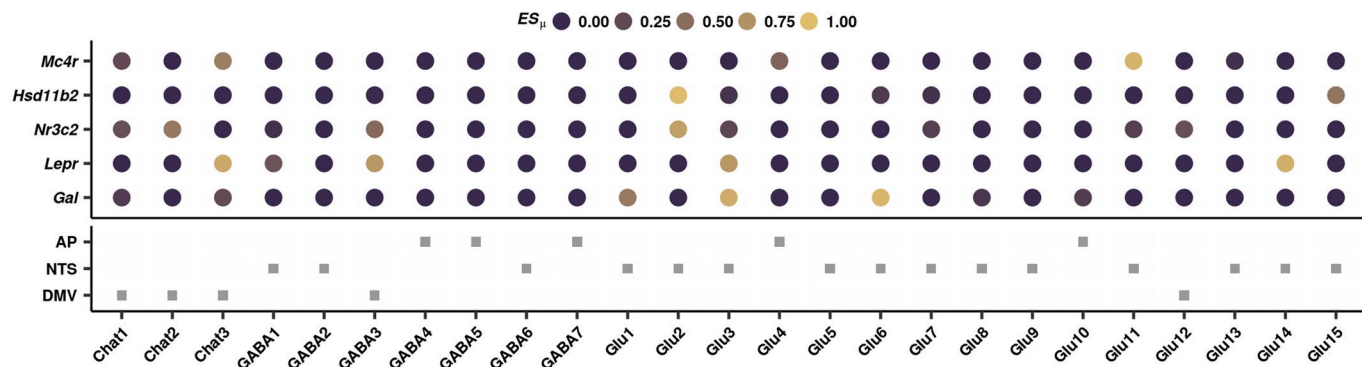
Extended Data Fig. 3 | Expression of DVC neuronal marker genes. **a**, Expression of marker genes for different neuronal populations. From top to bottom, dendrogram illustrating the similarity of the neuronal populations computed based on their gene expression levels, heatmap depicting the gene expression specificity values (ES_{μ}) of the neuronal marker genes, the most likely DVC origin of the neuronal populations. **b-z**, ISH of coronal brain sections (Allen Mouse Brain Atlas). N=1 mouse for all hybridizations except panels **m** and **o** (n=2 mice) and panel **p** (n=3 mice). Scale bar for panel **b** is representative for panels **c-z**, 100 μ m. Data for reconstruction of **a** are available in Supplementary Data 2.



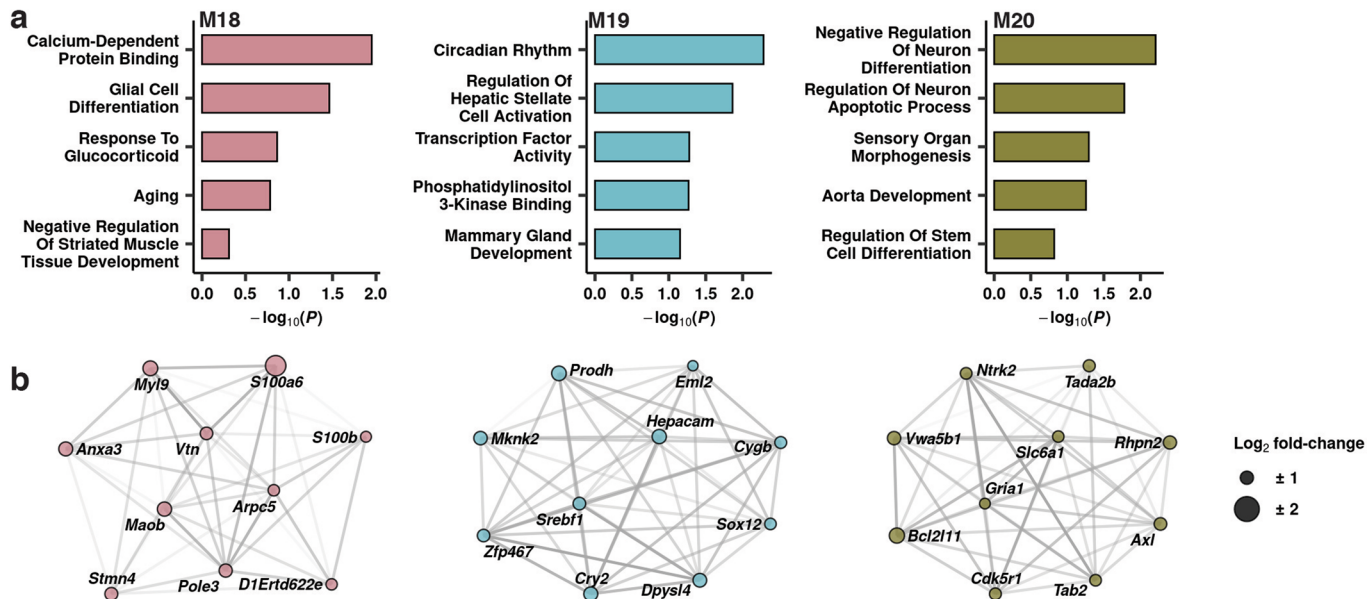
Extended Data Fig. 4 | Expression of appetite-suppressing receptors in mice and non-human primates. **a**, Representative image showing db-ISH of GFRALSR (blue) and GLP1R (red) in non-human primates (n=2). Scale bar, 250 µm. **b**, Representative image showing db-ISH of CALCR (blue) and GLP1R (red) in non-human primates (n=2). Scale bar, 100 µm. **c**, Representative image showing db-ISH of CASR (blue) and GLP1R (red) in non-human primates (n=2). Scale bar, 250 µm. **d**, Representative image showing db-ISH of Grpr (blue) and Calcr (red) in mice (n=4). Scale bar, 100 µm. **e**, Representative image showing db-ISH of Casr (blue) and Bdnf (red) in mice (n=4). Scale bar, 100 µm. **f**, Representative image showing db-ISH of Grpr (blue) and Bdnf (red) in mice (n=4). Scale bar, 100 µm. **g**, Representative image showing db-ISH of Casr (blue) and Mc4r (red) in mice (n=4). Scale bar, 100 µm. **h**, Representative image showing db-ISH of Grpr (blue) and Mc4r (red) in mice (n=4). Scale bar, 100 µm. **i-l**, Representative images showing TH (purple) or DDC (purple) immunoreactivity (green) and GFP immunoreactivity (green) in *Glp1r-Cre;GFP* or *Calcr-Cre;GFP* mice (n=3). Scale bar, 150 µm.



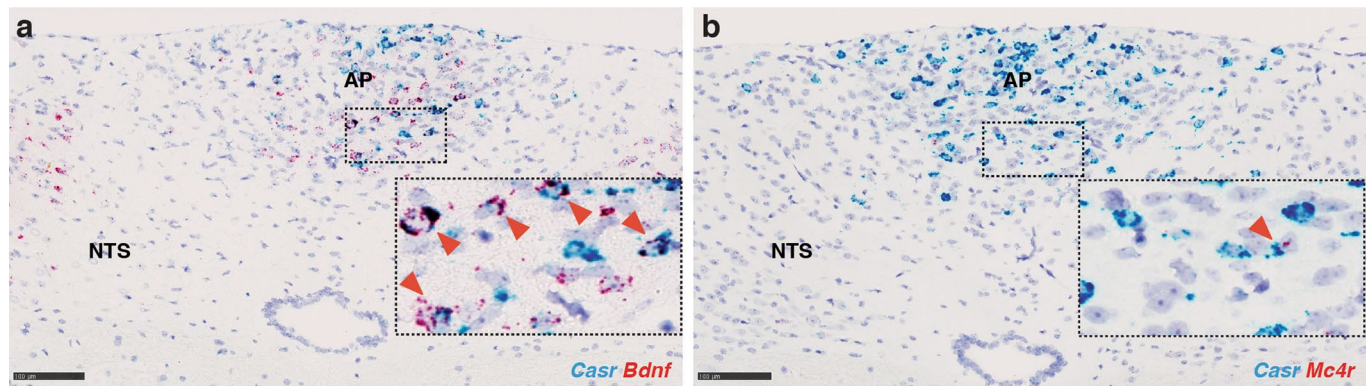
Extended Data Fig. 5 | Expression of appetite-suppressing receptors and peptides in mice and non-human primates. **a**, Representative image showing db-ISH of *CALCR* (blue) and *RAMP3* (red) in non-human primates (n=2). Scale bar, 100 µm. **b**, Representative image showing db-ISH of *Ccbe1* (blue) and *Gipr* (red) in mice (n=4). Scale bar, 100 µm. **c**, Representative image showing db-ISH of *Pax5* (blue) and *Gipr* (red) in mice (n=4). Scale bar, 100 µm. **d**, Representative image showing db-ISH of *Gipr* (blue) and *Glpr1r* (red) in mice (n=4). Scale bar, 100 µm. **e**, Representative image showing db-ISH of *Asb4* (blue) and *Gcg* (red) in mice (n=4). Scale bar, 100 µm.



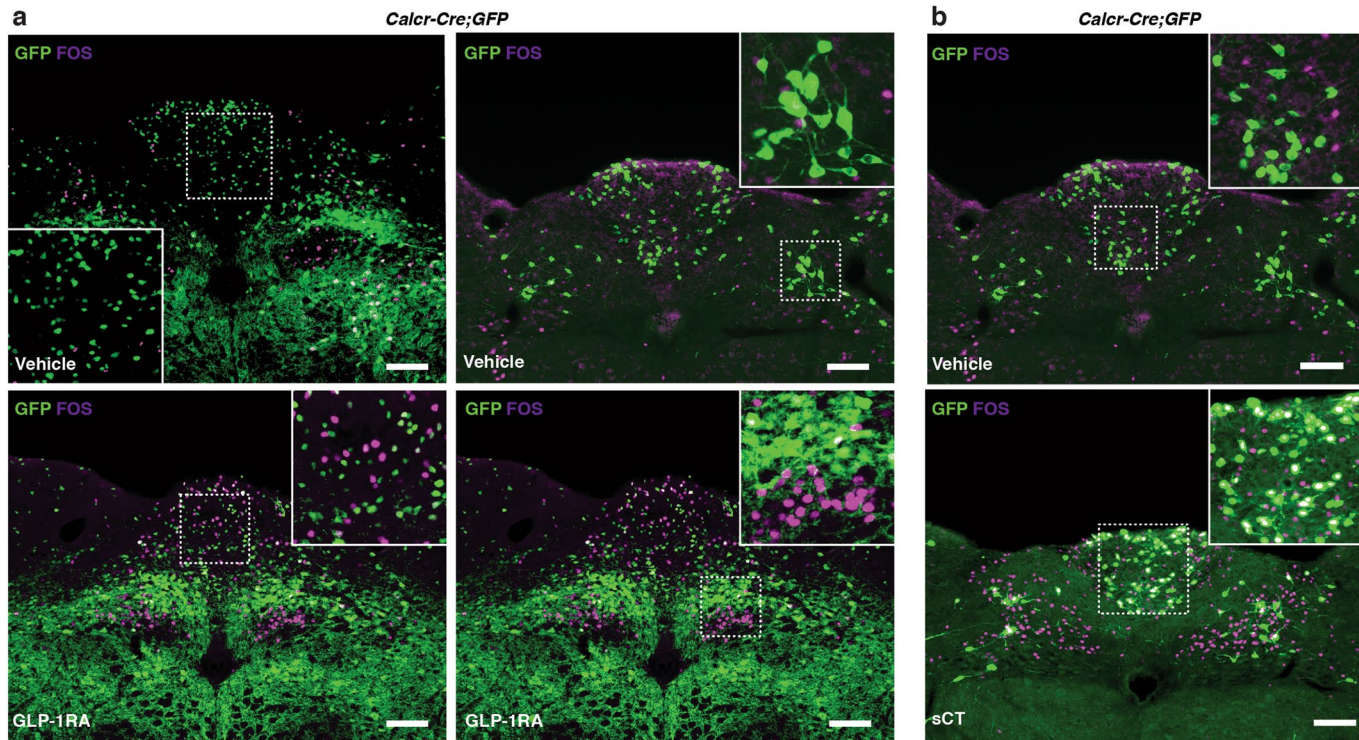
Extended Data Fig. 6 | Additional DVC neuronal populations with previously-defined functions. Expression of genes defining DVC neurons previously implicated in metabolic control. Top, expression specificity (ES_{μ}) of selected genes. Bottom, the most likely DVC origin of the neuronal populations. *Mc4r* cholinergic (*Chat3*) DMV neurons regulate circulating insulin³⁹, *Hsd11b2* and *Nr3c2* glutamatergic (*Glu2*) NTS neurons drive sodium appetite⁴⁰ and *Lepr* and *Gal* glutamatergic (*Glu3*) NTS neurons module breathing⁴¹. Data for reconstruction of figure are available in Supplementary Data 2.



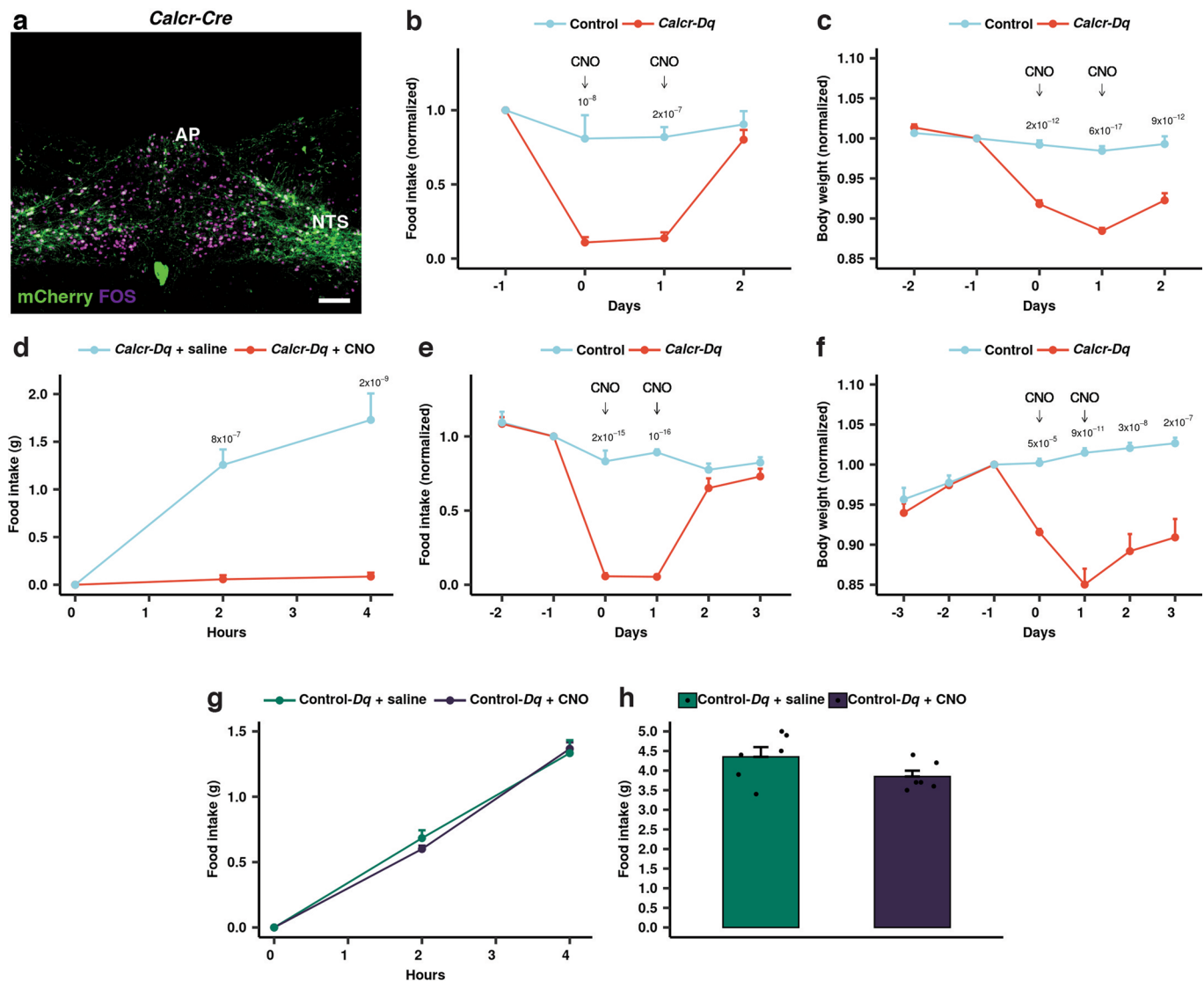
Extended Data Fig. 7 | GLP-1RA-downregulated modules. **a**, Most enriched Gene Ontology terms for modules M18–20. Bonferroni-adjusted g:Profiler P value. **b**, Top 10 genes for modules M18–20. Data for reconstruction of figure are available in Supplementary Data 1 and 4 and at NCBI GEO.



Extended Data Fig. 8 | Expression of *Bdnf* and *Mc4r* following GLP-1RA administration. **a**, Representative ic of *Castr* (blue) and *Mc4r* (red) in mice administered with Ex4 (i.v., 200 μ g kg $^{-1}$; n=2). Scale bar, 100 μ m. **b**, Representative image showing db-ISH of *Castr* (blue) and *Bdnf* (red) in mice administered with Ex4 (i.v., 200 μ g kg $^{-1}$; n=2). Scale bar, 100 μ m. i.v., intravenous.



Extended Data Fig. 9 | FOS immunoreactivity in *Calcr* AP and NTS cells following GLP-1RA or salmon calcitonin administration. **a**, Representative image showing FOS immunoreactivity (purple) and GFP immunoreactivity (green) in *Calcr*-Cre;GFP mice administered with Ex4 (i.p., 150 μ g kg $^{-1}$; n=3) or vehicle (n=3). Scale bar, 150 μ m. **b**, Representative image showing FOS immunoreactivity (purple) and GFP immunoreactivity (green) in *Calcr*-Cre;GFP mice administered with sCT (i.p., 150 μ g kg $^{-1}$; n=3) or vehicle (n=3). Scale bar, 150 μ m.



Extended Data Fig. 10 | Activation of *Calcr* NTS neurons suppresses feeding. **a**, Representative image showing mCherry immunoreactivity (pseudo-colored green) and FOS immunoreactivity (purple) after CNO treatment in *Calcr-Cre* mice injected with hM3Dq-mCherry in the NTS ($n=7$). Scale bar, 150 μ m. **b,c**, Long-term chow food intake (**b**) and body weight (**c**) in control ($n=6$) and *Calcr-Cre* mice injected with hM3Dq-mCherry in the NTS ($n=7$) measured during 1 day of saline, 2 days of CNO (i.p., 1 mg kg $^{-1}$) followed by 1 day of saline treatment. **d**, Short-term HFD food intake in *Calcr-Cre* mice injected with hM3Dq-mCherry in the NTS and treated with saline ($n=7$) or CNO (i.p., 1 mg kg $^{-1}$; $n=7$). **e,f**, Long-term HFD food intake (**e**) and body weight (**f**) in control ($n=5$) or *Calcr-Cre* mice injected with hM3Dq-mCherry in the NTS ($n=7$) measured during 3 days of saline, 2 days of CNO (i.p., 1 mg kg $^{-1}$) followed by 2 days of saline treatment. **g**, Short-term chow food intake in control mice injected with hM3Dq-mCherry in the NTS and treated with saline ($n=6$) or CNO (i.p., 1 mg kg $^{-1}$; $n=6$). Values are the mean \pm s.e.m. $P<0.05$ are specified, linear mixed effects model, Bonferroni-adjusted least squares means two-tailed t-test. **h**, Long-term chow food intake in control mice injected with hM3Dq-mCherry in the NTS and treated with saline ($n=6$) or CNO (i.p., 1 mg kg $^{-1}$; $n=6$). Values are the mean \pm s.e.m. Linear model, least squares means two-tailed t-test.

Reporting Summary

Nature Research wishes to improve the reproducibility of the work that we publish. This form provides structure for consistency and transparency in reporting. For further information on Nature Research policies, see our [Editorial Policies](#) and the [Editorial Policy Checklist](#).

Statistics

For all statistical analyses, confirm that the following items are present in the figure legend, table legend, main text, or Methods section.

n/a Confirmed

- The exact sample size (n) for each experimental group/condition, given as a discrete number and unit of measurement
- A statement on whether measurements were taken from distinct samples or whether the same sample was measured repeatedly
- The statistical test(s) used AND whether they are one- or two-sided
Only common tests should be described solely by name; describe more complex techniques in the Methods section.
- A description of all covariates tested
- A description of any assumptions or corrections, such as tests of normality and adjustment for multiple comparisons
- A full description of the statistical parameters including central tendency (e.g. means) or other basic estimates (e.g. regression coefficient) AND variation (e.g. standard deviation) or associated estimates of uncertainty (e.g. confidence intervals)
- For null hypothesis testing, the test statistic (e.g. F , t , r) with confidence intervals, effect sizes, degrees of freedom and P value noted
Give P values as exact values whenever suitable.
- For Bayesian analysis, information on the choice of priors and Markov chain Monte Carlo settings
- For hierarchical and complex designs, identification of the appropriate level for tests and full reporting of outcomes
- Estimates of effect sizes (e.g. Cohen's d , Pearson's r), indicating how they were calculated

Our web collection on [statistics for biologists](#) contains articles on many of the points above.

Software and code

Policy information about [availability of computer code](#)

Data collection No software was used for data collection.

Data analysis Bulk RNA-seq data was analyzed with bcl2fastq version 2.17.1.14, STAR version 2.5.2a, DESeq2, WGCNA, and gProfiler.
SnRNA-seq data was analyzed with 10x Genomics Cell Ranger version 3.0, DoubletFinder version 2.0.0, WGCNA, Seurat version 3.1.1, and CELLEX version 1.1.1.
SnATAC-seq data was analyzed with 10x Genomics Cell Ranger ATAC version 1.1.0, SnapATAC version 1.0.0, MACS2 version 2.2.6, Signac version 0.1.5, Seurat version 3.1.1, and ChromVar.
Genetic enrichment analysis was carried out using CELLECT version 1.0.0.
For a list of all code used to analyze the data please refer to: <https://github.com/perslab/Ludwig-2021>.

For manuscripts utilizing custom algorithms or software that are central to the research but not yet described in published literature, software must be made available to editors and reviewers. We strongly encourage code deposition in a community repository (e.g. GitHub). See the Nature Research [guidelines for submitting code & software](#) for further information.

Data

Policy information about [availability of data](#)

All manuscripts must include a [data availability statement](#). This statement should provide the following information, where applicable:

- Accession codes, unique identifiers, or web links for publicly available datasets
- A list of figures that have associated raw data
- A description of any restrictions on data availability

All genetic data generated in this study (bulk RNA-seq, snRNA-seq and snATAC-seq) are available in GEO under SuperSeries accession number GSE166649.

All other data are available from the authors upon reasonable request.
The PolyA_DB database version 3.2 used in the manuscript is available at https://exon.apps.wistar.org/PolyA_DB/v3/.

Field-specific reporting

Please select the one below that is the best fit for your research. If you are not sure, read the appropriate sections before making your selection.

Life sciences Behavioural & social sciences Ecological, evolutionary & environmental sciences

For a reference copy of the document with all sections, see nature.com/documents/nr-reporting-summary-flat.pdf

Life sciences study design

All studies must disclose on these points even when the disclosure is negative.

Sample size	For the bulk RNA-seq, the number of animals per group was estimated based on variance studies in former RNA-seq studies performed by the Novo Nordisk A/S test facilities. Using the R RnaSeqSampleSize library version 1.6 with default parameters it was estimated that n=15 animals per group resulted in 90% power to identify a 2-fold change at a false-discovery rate of 5%. For the single-nucleus sequencing study, the number of animals (n=5-7) were based on previous studies from brain single-cell RNA-seq data (reference: https://www.nature.com/articles/s41467-020-17720-5).
Data exclusions	For the bulk RNA-seq data set, a few samples were excluded due to poor tissue morphology or unsuccessful cDNA library generation. For the snRNA-seq data, n=10 animals were administered with GLP-1RA as technical errors such as dissection of tissue could result in reduced sample size. A few data points were missing when collecting food intake and birth weight from some of the animals. Animals were selected from each group that included confirmation of correct tissue dissection.
Replication	Change of body weight and food intake in mice following GLP-1RA administration has been repeated at least four times at the Novo Nordisk A/S test facilities with consistent reproducibility. For the bulk and single-nucleus sequencing data, we have made raw data files and code used to analyze data publicly available (see above). For the DREADD experiments, animals were perfused and the brains were dissected to verify viral injections. Brains with off-target hits that showed mCherry leaking to neighboring areas were excluded. For the DREADD mouse experiment, no data was excluded. For the DREAEDD rat experiment, two rats were excluded due to spread of the virus to neighboring areas.
Randomization	For the bulk and single-nucleus sequencing experiments, one day before study start animals were block-randomized based on body weight.
Blinding	During the in vivo part of the bulk and single-nucleus sequencing studies, animals were assigned ID numbers rather than group names. Administration of compounds was not blinded but done by staff ignorant to the final aim of the study. During tissue processing (LCM and mRNA) only the individual animal ID was recorded ensuring some degree of blinding. The DREADD experiments were not blinded as there was only one experimenter conducting surgeries and experiments.

Reporting for specific materials, systems and methods

We require information from authors about some types of materials, experimental systems and methods used in many studies. Here, indicate whether each material, system or method listed is relevant to your study. If you are not sure if a list item applies to your research, read the appropriate section before selecting a response.

Materials & experimental systems

n/a	Involved in the study
<input type="checkbox"/>	<input checked="" type="checkbox"/> Antibodies
<input checked="" type="checkbox"/>	<input type="checkbox"/> Eukaryotic cell lines
<input checked="" type="checkbox"/>	<input type="checkbox"/> Palaeontology and archaeology
<input type="checkbox"/>	<input checked="" type="checkbox"/> Animals and other organisms
<input checked="" type="checkbox"/>	<input type="checkbox"/> Human research participants
<input checked="" type="checkbox"/>	<input type="checkbox"/> Clinical data
<input checked="" type="checkbox"/>	<input type="checkbox"/> Dual use research of concern

Methods

n/a	Involved in the study
<input checked="" type="checkbox"/>	<input type="checkbox"/> ChIP-seq
<input checked="" type="checkbox"/>	<input type="checkbox"/> Flow cytometry
<input checked="" type="checkbox"/>	<input type="checkbox"/> MRI-based neuroimaging

Antibodies

Antibodies used

Antibody used	Applicable Supplier name Catalog number Clone name Lot number
	FOS ELISA, ICC, IHC, WB, IF Cell Signaling Technology #2250 not applicable 10
	GFP ELISA, ICC, IHC, WB Aves Laboratories GFP1020 not applicable GFP697986
	dsRed WB, IP, IL Takara 632496 not applicable 1904182
	TH WB, Simple Western, ICC/IF, IHC, IHC-Fr, IHC-P, Dual ISH-IHC, IHC-FrFl, IHC-WhMt, KO Novus Biologicals NB300-109 not applicable ajo8186
	DDC WB, IP, IHC, IF, ELISA Proteintech 10166-1-AP not applicable 00000353
	Alexa Flur 488 Flow, ICC, IHC, IF, Misc Thermo Fisher A11039 2079383

Alexa Flur 568 Flow, ICC, IHC, IF, Misc Thermo Fisher A10042 2044343
 Alexa Flur 647 Flow, ICC, IHC, IF, Misc Thermo Fisher A-31573 2083195
 GLP1R IHC Abcam ab218532 EPR21819 GR3246505-4

Validation

Antibody used Validation Validation website with reference
 FOS Used for mouse brain section, 1:1000 dilution <https://www.cellsignal.com/products/primary-antibodies/c-fos-9f6-rabbit-mab/2250>
 GFP Used for mouse brain section, 1:1000 dilution <https://www.aveslabs.com/collections/epitope-tag-6xhis-beta-gal-actin-and-gfp-antibodies/products/green-fluorescent-protein-gfp-antibody>
 dsRed Used for mouse brain section, 1:1000 dilution <https://www.takarabio.com/products/antibodies-and-elisa/fluorescent-protein-antibodies/red-fluorescent-protein-antibodies>
 TH Used for mouse brain section, 1:1000 dilution https://www.novusbio.com/products/tyrosine-hydroxylase-antibody_nb300-109
 DDC Used for mouse brain section, 1:1000 dilution <https://www.ptglab.com/products/DDC-Antibody-10166-1-AP.htm>
 Alexa Flur 488 Used for mouse brain section, 1:200 dilution <https://www.thermofisher.com/antibody/product/Goat-anti-Chicken-IgY-H-L-Secondary-Antibody-Polyclonal/A-11039>
 Alexa Flur 568 Used for mouse brain section, 1:200 dilution <https://www.thermofisher.com/antibody/product/Donkey-anti-Rabbit-IgG-H-L-Highly-Cross-Adsorbed-Secondary-Antibody-Polyclonal/A10042>
 Alexa Flur 647 Used for mouse brain section, 1:200 dilution <https://www.thermofisher.com/antibody/product/Donkey-anti-Rabbit-IgG-H-L-Highly-Cross-Adsorbed-Secondary-Antibody-Polyclonal/A-31573>
 GLP1R Used for mouse brain section, 1:200 dilution <https://www.citeab.com/antibodies/6158544-ab218532-anti-glp1r-antibody-epc21819>

Animals and other organisms

Policy information about [studies involving animals](#); [ARRIVE guidelines](#) recommended for reporting animal research

Laboratory animals

Laboratory animals used to generated the RNA-seq were C57BL/6 male mice between 31-weeks of age at day 0 (bulk RNA-seq) and 26-weeks at day 0 (single-nucleus RNA- and ATAC-seq).
 Laboratory animals used for the DREADD experiments were Calcr-Cre male mice between were eight-12 weeks of age at day 0 and Calcr-Cre female rats between six-12 months of age at day 0.

Wild animals

No wild animals were used in this study.

Field-collected samples

No field-collected samples were used in this study.

Ethics oversight

All in vivo experiments used to generate the bulk and single-nucleus sequencing data were conducted in accordance with internationally accepted principles for the care and use of laboratory animals approved by the Danish Ethical Committee for Animal Research.
 For the DREADD experiments, all procedures performed were approved by the University of Michigan Committee on the Use and Care of Animals and in accordance with Association for the Assessment and Approval of Laboratory Animal Care and National Institutes of Health guidelines.

Note that full information on the approval of the study protocol must also be provided in the manuscript.